

CHEM: Estimating and Understanding Hallucinations in Deep Learning for Image Processing

Jianfei Li^{1,*}

lijianfei@math.lmu.de

Ines Rosellon-Inclan^{1,2}

rosellon@math.lmu.de

Gitta Kutyniok^{1,2,3,4}

kutyniok@math.lmu.de

Jean-Luc Starck^{5,6}

jstarck@cea.fr

Abstract

U-Net and other U-shaped architectures have achieved significant success in image deconvolution tasks. However, challenges have emerged, as these methods might generate unrealistic artifacts or hallucinations, which can interfere with analysis in safety-critical scenarios. This paper introduces a novel approach for quantifying and comprehending hallucination artifacts to ensure trustworthy computer vision models. Our method, termed the Conformal Hallucination Estimation Metric (CHEM), is applicable to any image reconstruction model, enabling efficient identification and quantification of hallucination artifacts. It offers two key advantages: it leverages wavelet and shearlet representations to efficiently extract hallucinations of image features and uses conformalized quantile regression to assess hallucination levels in a distribution-free manner. Furthermore, from an approximation theoretical perspective, we explore the reasons why U-shaped networks are prone to hallucinations. We test the proposed approach on the CANDELS astronomical image dataset with models such as U-Net, Swin-UNet, and Learnlets, and provide new perspectives on hallucination from different aspects in deep learning-based image processing.

1 Introduction

In recent decades, artificial intelligence has permeated nearly every domain, including medical diagnosis pipelines [29], autonomous driving [62], natural language processing

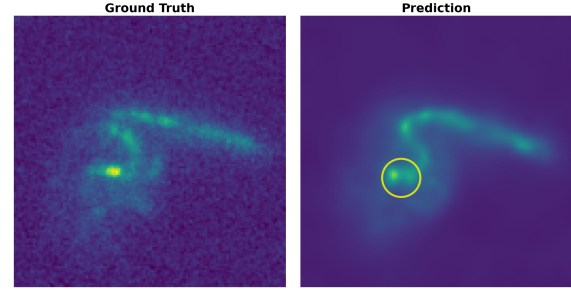


Figure 1. An example of hallucinations in astronomical image deconvolution obtained from U-Net predictions.

[21], and speech recognition [41], among others. Despite these advances, hallucinations have emerged as a recurring challenge accompanying the success of deep learning. The phenomenon of hallucination has been observed in a wide range of deep learning models, including Large Language Models [61], Large Vision-Language Models [36], Natural Language Generation systems [26], and Large Foundation Models [50].

Specifically, the hallucination phenomenon has been observed in image processing [17], raising concerns in medical imaging [8, 58] and in the natural sciences [2, 7]. Figure 1 illustrates that hallucinations appear in astronomical image deconvolution tasks [2]. In informal terms, hallucinations refer to realistic textures in predictions that are missing from the ground-truth images. Despite recent efforts to formalize hallucinations in imaging tasks [8, 58], there is no consensus on a common framework to quantify hallucinations. In addition to measuring hallucinations, another key challenge is to identify the fundamental issue that leads to these hallucinations. Both understanding and estimating the confidence of the model in its outputs are crucial, as unreliable predictions can lead to misdiagnosis or erroneous decision-making [12]. Given that textures often play a more significant and noticeable role than individual pixels, a hallucination detection algorithm should be designed

¹Ludwig-Maximilians-Universität München, Munich, Germany

²Munich Center for Machine Learning (MCML), Germany

³University of Tromsø, Norway

⁴German Aerospace Center (DLR), Germany

⁵Université Paris-Saclay, Université Paris Cité, CEA, CNRS, AIM, France

⁶Foundation for Research and Technology Hellas (FORTH), Greece

*Corresponding author

to be sensitive to artifacts in textures.

This paper focuses on providing a comprehensive analysis to assess and understand hallucination in image processing tasks. We begin by introducing a novel texture-level hallucination detection algorithm for image processing. To successfully capture texture hallucinations, we use wavelets and shearlets to extract directional detail from images. Given the significance of U-Net and its variations in image processing tasks, we then analyze the reasons why U-shaped architectures tend to produce hallucinations, utilizing approximation theory. Finally, we conduct numerical experiments on the CANDELS dataset [18, 27] using U-Net, SwinUNet, and Learnlets. This application represents a particularly important case: while technological advances are producing unprecedented amounts of data, it is equally crucial that reconstruction methods remain reliable, as such reconstruction tasks are safety-critical, where spurious details can lead to misleading interpretations.

Our contributions are outlined as follows:

- **Hallucination quantification:** We introduce a novel hallucination detection approach: **Conformal Hallucination Estimation Metric (CHEM)**. Our method is designed to efficiently capture implausible but realistic textures by wavelets/shearlets, and we do not require prior knowledge on the underlying distributions of images, which makes our algorithm efficient.
- **Critical factors behind hallucinations:** Based on approximation theory, we offer a comprehensive analysis of the reasons behind hallucinations in deep learning methods. The key factors include the model’s limited parameters and the properties of input images. Our result also characterizes the expressivity of U-shaped networks for general image processing tasks.
- **Experimental Results:** We analyze the impact of different dictionaries (wavelets, shearlets), loss functions (ℓ_1 , ℓ_2), and training epochs. Two main findings emerged: (i) there is a tradeoff between accuracy and hallucination, and (ii) models with similar accuracy exhibit different robustness to input perturbations. This work offers new insights into the evaluation of deep learning models in imaging and potentially paves the way to new methodologies to design deep learning techniques or reduce model hallucination in image processing.

The source code for the experiments will be made publicly available.

2 Related Work

Hallucinations in imaging: Deep learning-based approaches in image processing tasks have been reported to introduce undesired effects. The work [12] established a fundamental trade-off in generative image restoration: improving perceptual quality inevitably increases uncertainty. In medical imaging, hallucinations have been identified as

a major concern in integrating deep learning into the image reconstruction pipeline [8, 44]. To understand the underlying mechanisms responsible for hallucinations, theoretical foundations were developed in [17], revealing their prevalence in deep learning models. The study also indicated that achieving an optimal image reconstruction method during training might be impossible.

Hallucination measurements: While hallucinations in image processing have been documented, methods for their assessment remain limited. We refer the reader to the following works for a detailed overview. Hallucinations in ill-posed inverse problems are conceptualized using *hallucination maps*, which serve to pinpoint features that are demonstrably absent from the measurements [8]. This method was developed for MRI, where the imaging operator is known. Subsequent research suggests comparing reconstruction processes with zero-hallucination references (or forward processes) in generative reconstruction models under Hellinger distance [58]. However, their approach requires density estimations and is simplified by assuming that those processes can be approximated well by multivariate normal distributions. In explainability studies, hallucinations are noted in attribution masks. A *Hallucination Score* quantifies them as the ratio of edges appearing solely in the explanation to those in an input image [28]. This metric is tailored for analyzing the decision-making process in image classification models rather than hallucinations in image reconstruction tasks. In galaxy image deconvolution, the *hallucination rate* is defined as the difference between objects and clumps derived from SCARLET [2]. Centroids of a detection outside five pixels from those in ground-truth images are considered hallucinations. Though suitable for galaxy images, this method may introduce bias with SCARLET and does not account for object shape or detailed texture variations.

U-shaped networks: The original U-Net architecture, introduced by Ronneberger et al. (2015) [49], which comprises a contracting encoder for hierarchical feature extraction and an expansive decoder for resolution recovery, coupled with skip connections, enabled breakthroughs in a wide range of fields, such as medical imaging [24] or autonomous driving [62]. Enhancing the learning capacity of U-Net can be achieved by implementing a bottleneck between the encoding path and the decoding path [9, 10, 34, 63]. This design philosophy inspired variants tailored to diverse tasks. Contemporary U-Net derivatives largely fall into three categories: (i) architectural reconfigurations, such as U-Net++ [63] and U²-Net [46] with nested skip pathways, (ii) operator replacements that exchange convolutions with wavelets (MWCNN [37]), transformers (TransUNet [10], Swin-UNet [9]) or state-space Mamba blocks (U-Mamba [39]); (iii) multi-scale context aggregation, e.g., DeepLabv3+ [11] with atrous convolu-

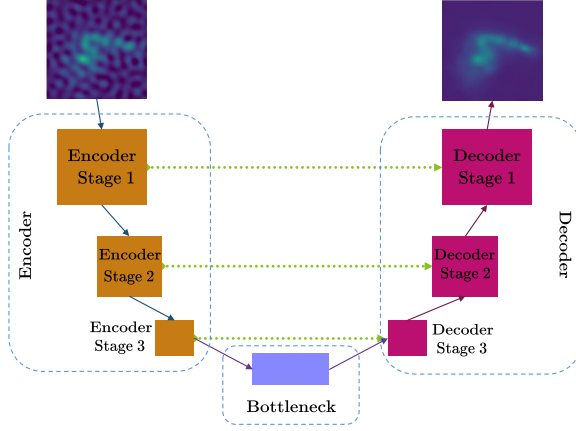


Figure 2. U-shaped network architectures. The foundational components, namely the encoder stages, decoder stages, and the bottleneck, can be built from convolutional layers, attention layers, or transformer architectures.

tions and attention-augmented frameworks like Attention U-Net [45] that refine spatial focus. Figure 2 illustrates the general structure of U-shaped architectures.

3 Methodology

3.1 Notations

Let \mathbb{R} , \mathbb{R}_+ , \mathbb{N} , and \mathbb{N}_+ denote the sets of real numbers, positive numbers, nonnegative integers, and positive integers, respectively. We denote $[N] := \{1, \dots, N\}$ if $N \in \mathbb{N}_+$. For $x \in \mathbb{R}^d$, we denote its i -th element as x_i or $(x)_i$. We denote $\|\cdot\|_p$, $p \in [1, \infty]$ as the vector norm. Let $\Omega[-1, 1]^d$. The $L_p(\Omega)$ space contains measurable functions that have a finite L_p norm $\|f\|_{L_p(\Omega)} = (\int_{\Omega} |f(x)|^p dx)^{1/p} < \infty$. For $p = \infty$, we define $\|f\|_{L_{\infty}(\Omega)} := \text{ess sup } |f|$.

3.2 Mathematical formulation of hallucinations

In applications, our objective is to construct a neural network $\Phi(x) := \Phi(x; w)$, parameterized by some weights organized into a vector w . Consider \mathcal{X} and \mathcal{Y} to be sets of discrete images. Then the network aims to approximate an unknown mapping $\mathcal{M} : \mathcal{X} \rightarrow \mathcal{Y}$, which describes a complex relationship between the input space \mathcal{X} and the output space \mathcal{Y} .

We now provide the intuition underlying our definition. Consider a set $B_{\alpha}(\Phi(X)) \subset \mathcal{Y}$, consisting of $\Phi(X)$ and images in \mathcal{Y} that are similar to $\Phi(X)$. Furthermore, we assume that, with a probability of at least $1 - \alpha$, it includes the true image $\mathcal{M}(X)$, for a small α . This naturally indicates the occurrence of hallucinations if $\mathcal{M}(X) \notin B_{\alpha}(\Phi(X))$. Hence, when hallucinations occur, any image from $B_{\alpha}(\Phi(X))$ is far from the ground truth image $\mathcal{M}(X)$. This suggests that the prediction $\Phi(X)$ is unlikely to accurately depict $\mathcal{M}(X)$.

and therefore contains hallucinated textures.

Assume that there exist hallucinations in a neural network Φ at X . The magnitude of the hallucination level can be defined as $\text{dist}(\mathcal{M}(X), B_{\alpha}(\Phi(X)))$, which measures the distance between the ground truth and any image similar to the prediction with respect to α . Here we denote by $\text{dist}(\cdot, \cdot) : \mathcal{Y} \times \mathcal{Y} \rightarrow \mathbb{R}$ a metric such that $\text{dist}(Y_1, Y_2) = 0$ when $Y_1 = Y_2$. For any subset $A \subset \mathcal{Y}$, we denote $\text{dist}(Y, A)$ as $\text{dist}(Y, A) := \inf_{Z \in A} \text{dist}(Y, Z)$. In the absence of hallucination, the true value $\mathcal{M}(X)$ is contained within $B_{\alpha}(\Phi(X))$, resulting in a hallucination measurement of zero. In contrast, when hallucinations are present, the distance turns positive, allowing us to quantify the expected value of this distance as the degree of hallucination of the model Φ for performing \mathcal{M} .

Definition 3.1. Let $\alpha \in (0, 1)$ and \mathbb{P} be a probability measure over \mathcal{X} . For a learning task $\mathcal{M} : \mathcal{X} \rightarrow \mathcal{Y}$, we define the hallucination of a neural network $\Phi(\cdot)$ for a randomly sampled data pair $(X, Y) := (X, \mathcal{M}(X))$ as

$$H(\Phi; \alpha) := H(\Phi) := \mathbb{E} \text{dist}(Y, B_{\alpha}(\Phi(X))), \quad (1)$$

where $B_{\alpha}(\Phi(X))$ is given by

$$\mathbb{P}(Y \in B_{\alpha}(\Phi(X))) \geq 1 - \alpha. \quad (2)$$

Remark 3.2. In in-context learning with generative AI, the hallucination rate proposed in [25] is defined similarly to Definition 3.1, where $\text{dist}(Y, B_{\alpha}(\Phi(X))) := \chi_{\{Y \notin B_{\alpha}(\Phi(X))\}}$, with $\chi_A(x) = 1$ if x belongs to A and zero otherwise. An analogous characterization of hallucination for image processing was explored in [3] and subsequently improved in [30], enabling the identification of reliable regions in predicted images.

3.3 Conformal hallucination estimation metric

In the following, we develop an algorithm to assess hallucinations as defined in Definition 3.1. For image processing tasks, an ideal hallucination measurement should efficiently capture plausible but inconsistent textures during inference. Wavelets and shearlets have been shown as powerful dictionaries in image processing [20, 31, 32, 34, 40]. Their ability to extract directional texture information makes them ideal tools for detecting hallucinations. Let $X \in \mathcal{X} \subset \mathbb{R}^{t_1}$, $Y \in \mathcal{Y} \subset \mathbb{R}^{t_2}$. Here, we flatten the images into vectors for simplicity. We refer to W as either a discrete wavelet transform (DWT) or a discrete shearlet transform (DST). For an in-depth overview of wavelets and shearlets, please refer to the appendix. The texture information is contained in $\hat{X} := WX \in \mathbb{R}^{\hat{t}_1}$ for a certain \hat{t}_1 determined by W . Each i -th element in \hat{X} contains different directional texture information in X . In the output space \mathcal{Y} , we can similarly compute texture information of Y by a DWT/DST, denoted as $\hat{Y} \in \mathbb{R}^{\hat{t}_2}$.

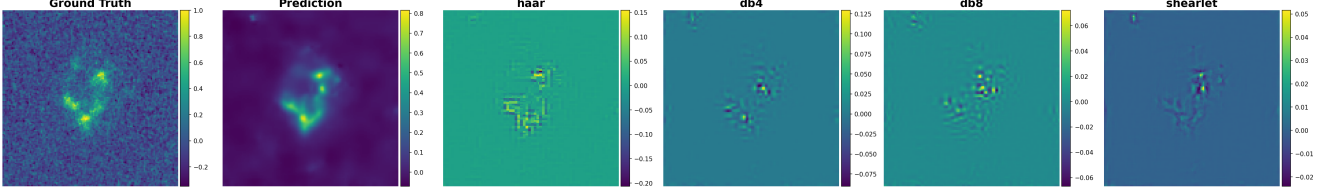


Figure 3. Quantifying hallucinations of a U-Net trained with ℓ_2 loss on astronomical images using different dictionaries. Visually, db8 and shearlets provide a clearer representation of the hallucinations present in the prediction. The reconstructions correspond to the fine-scale coefficients of these dictionaries with high CHEM values. For details, please refer to Section 5 (Evaluation Details).

To detect hallucinations in the wavelet or shearlet domain, our objective is to estimate a mapping $\hat{R}(X)$ such that the interval centered at $(\widehat{\Phi(X)})_j$ with radius $\hat{R}(X)_j$ gathers comparable directional textures surrounding $\widehat{\Phi(X)}_j$

$$B_\alpha \left(\widehat{\Phi(X)}_j \right) := \left[\widehat{\Phi(X)}_j - \hat{R}(X)_j, \widehat{\Phi(X)}_j + \hat{R}(X)_j \right], \quad (3)$$

and the actual value is likely to lie within this interval with high probability

$$\mathbb{P} \left((\hat{Y})_j \in B_\alpha \left(\widehat{\Phi(X)}_j \right) \right) \geq 1 - \alpha. \quad (4)$$

This characterizes confidence intervals with a mapping $\hat{R} : \mathbb{R}^{t_1} \rightarrow \mathbb{R}^{t_2}$. Let us choose the metric function as $\text{dist}(Y_1, Y_2) := \frac{1}{t_2} \sum_{j=1}^{t_2} |(\widehat{Y_1})_j - (\widehat{Y_2})_j|$ for $(Y_1, Y_2) \in \mathcal{Y} \times \mathcal{Y}$ and $B_\alpha \left(\widehat{\Phi(X)} \right) := \prod_{j=1}^{t_2} B_\alpha \left(\widehat{\Phi(X)}_j \right)$. Then Definition 3.1 for measuring hallucination over a whole predicted image can be equivalently rewritten by averaging texture-wise hallucination scores

$$H(\Phi) := \frac{1}{\hat{t}_2} \sum_{j=1}^{\hat{t}_2} H(\Phi)_j, \quad (5)$$

where the degree of hallucination at the j -th directional texture information is given by

$$\begin{aligned} H(\Phi)_j &= \mathbb{E} \text{dist} \left((\hat{Y})_j, B_\alpha \left(\widehat{\Phi(X)}_j \right) \right) \\ &= \mathbb{E} \left(|(\widehat{\Phi(X)}_j - (\hat{Y})_j| - \hat{R}(X)_j \right)_+, \end{aligned} \quad (6)$$

with $(z)_+ := \max\{z, 0\}$ for any $z \in \mathbb{R}$. In this context, α represents the level of confidence associated with each texture hallucination and can be readily extended to define the overall image confidence as that in Definition 3.1. Our hallucination measurements (5) and (6) are named the *Conformal Hallucination Estimation Metric* (CHEM).

Let $\hat{r}(\cdot) : \mathbb{R}^{t_1} \rightarrow \mathbb{R}^{\hat{t}_2}$ be an initialization of $\hat{R}(\cdot)$. The remaining unresolved issue is figuring out how to modify an initial radius $\hat{r}(X)$ to reach a target radius $\hat{R}(X)$, while ensuring the condition (4) is met. This goal can be achieved by

using conformal quantile regression proposed in [33] without strong distributional assumptions. Given a finite calibration dataset $\{(X_n, Y_n) \in \mathcal{X} \times \mathcal{Y}\}_{n=1}^N$. We define $\hat{R}(X)_j$ as $\hat{R}(X)_j := g_\lambda(\hat{r}(X)_j)$, where $g_\lambda : \mathbb{R}_+ \rightarrow \mathbb{R}_+$ denotes a non-decreasing calibration function with $\lambda \in [a, b]$. We choose λ_j as the $(1 - \alpha)(1 + 1/N)$ -th empirical quantile of $\{\lambda_j^n\}_{n=1}^N$, where

$$\lambda_j^n := \inf \left\{ \lambda \in [a, b] : g_\lambda(\hat{r}(X_n)_j) \geq \left| \widehat{\Phi(X_n)}_j - (\widehat{Y_n})_j \right| \right\}. \quad (7)$$

Here, λ_j^n is equal to a (or b) when the condition is always (or never) met. Let (X, Y) be a new data sample. According to [33, Proposition 1], if the samples $\mathcal{D} \cup \{(X, Y)\}$ are independently drawn from an unknown distribution μ on $\mathcal{X} \times \mathcal{Y}$, then it demonstrates that

$$\alpha - \frac{1}{N+1} \leq \mathbb{P} \left((\hat{Y})_j \notin B_\alpha \left(\widehat{\Phi(X)}_j \right) \right) \leq \alpha. \quad (8)$$

To assess hallucinations throughout an entire image, we set an upper bound θ in (6). This ensures that the evaluation of hallucinations across the whole image is not disproportionately affected by hallucination at an individual texture. Hence, we define

$$H^\theta(X, Y)_j := \min \left\{ \left(|(\widehat{\Phi(X)}_j - (\hat{Y})_j| - \hat{R}(X)_j \right)_+, \theta \right\}, \quad (9)$$

for some $\theta > 0$. The extent of hallucination detected in the wavelet or shearlet domain is ultimately defined by $H^\theta(\Phi)_j$ and $H^\theta(\Phi)$

$$H^\theta(\Phi)_j := \mathbb{E} H^\theta(X, Y)_j, \quad H^\theta(\Phi) := \frac{1}{\hat{t}_2} \sum_{j=1}^{\hat{t}_2} H^\theta(\Phi)_j, \quad (10)$$

for some $\theta > 0$. In Figure 3, we illustrate the effect of combining CHEM with different dictionaries, specifically Haar, db4, and db8 wavelets [14], and shearlets. The following result shows that, for application purposes, it suffices to evaluate CHEM using finitely many samples. Subsequently, we illustrate the complete procedure in Algorithm 1.

Proposition 3.3. Let $\theta \in \mathbb{R}_+$ and $\mathcal{D} \cup \{(X_m, Y_m)\}_{m=1}^M$ be independent and identically distributed random variables. Then, with probability at least $1 - \delta$, the following inequality holds

$$\left| H^\theta(\Phi)_j - \frac{1}{M} \sum_{m=1}^M H^\theta(X_m, Y_m)_j \right| \leq \frac{\sqrt{\theta^2 \log(2/\delta)}}{\sqrt{2M}}. \quad (11)$$

In addition, under the same condition, the inequality

$$\left| H^\theta(\Phi) - \frac{1}{M} \sum_{m=1}^M \frac{1}{\hat{t}_2} \sum_{j=1}^{\hat{t}_2} H^\theta(X_m, Y_m)_j \right| \leq \frac{\sqrt{\theta^2 \log(2/\delta)}}{\sqrt{2M}}. \quad (12)$$

holds with probability at least $1 - \delta$.

Remark 3.4. Conformal prediction has recently received great attention for uncertainty quantification, which is used to characterize $B_\alpha(\cdot)$. In [57], a specific approach considering organ-dependence was examined, which required a segmentation model to pinpoint organs in computed tomography data. However, this requires additional effort in creating a segmentation model that is meaningful for the task. In image-to-image problems, the risk-controlling prediction set (RCPS) was also used to estimate $B_\alpha(\cdot)$. As noted in [33], CQR typically yields tighter intervals and thus sharper uncertainty estimates. Extending [48], the authors of [33] apply CQR pixelwise to inverse problems and evaluate the miscoverage rate and interval width. In weak-lensing mass mapping, they relate a higher uncertainty to high-density regions via the distance between predictions and intervals. We extend this direction by enabling uncertainty assessment in the wavelet/shearlet domain. This offers a more detailed description of hallucinations.

Algorithm 1 Conformal Hallucination Estimation Metric

Require: Test set $\mathcal{D}_1 = \{(X_m, Y_m)\}_{m=1}^M$, calibration set $\mathcal{D}_2 = \{(X_n, Y_n)\}_{n=1}^N$, network Φ , g_λ , DWT/DST W , confidence level α , radius \hat{r} , threshold θ ;

- 1: **for all** $j = 1, \dots, \hat{t}_2$ **do**
- 2: **for all** $n = 1, \dots, N$ **do**
- 3: Solve λ_j^n in (7)
- 4: **end for**
- 5: $\lambda_j \leftarrow (1 - \alpha)(1 + 1/N)$ -th empirical quantile of $\{\lambda_j^n\}_{n=1}^N$
- 6: $\hat{R}(\cdot)_j \leftarrow g_{\lambda_j}(\hat{r}(\cdot)_j)$
- 7: **end for**
- 8: **for all** $m = 1, \dots, M$ **do**
- 9: Compute $H^\theta(X_m, Y_m)_j$ using (9)
- 10: **end for**
- 11: $H^\theta(\Phi) \leftarrow \frac{1}{M} \sum_{m=1}^M \frac{1}{\hat{t}_2} \sum_{j=1}^{\hat{t}_2} H^\theta(X_m, Y_m)_j$
- 12: **Output:** CHEM $H^\theta(\Phi)$

4 Understanding the Causes of Hallucinations

For the ground truth mapping \mathcal{M} it obviously holds $H(\mathcal{M}) = 0$ since $B_\alpha(\mathcal{M}(\cdot)) \supset \{\mathcal{M}(\cdot)\}$ for any α . This means that there is at least one mapping that never hallucinates. This brings us to the question: Does there exist a neural network that never hallucinates, or $\Phi(\cdot) = \mathcal{M}(\cdot)$ almost everywhere? And if such a network does not exist, what causes hallucinations in its predictions? This question corresponds to grasping the boundary of $B_\alpha(\Phi(X))$, which differentiates between hallucinated and non-hallucinated cases. Investigating the causes of hallucinations not only offers a deeper insight into the capacity of neural networks, but could also potentially generate new strategies to eliminate them.

Since images can be regarded as discrete representations of real-world scenes [4], in this section, we consider learning a general mapping $\mathcal{M} : \mathcal{C}(\Omega) \rightarrow \mathcal{C}(\Omega)$ with U-shaped networks where $\mathcal{C}(\Omega)$ contains all continuous functions. Therefore, the discussion will include an examination of the discretization error to provide a better understanding of hallucination, which is more directly related to real-world scenes.

Let $\xi := \{\xi_1, \xi_2, \dots, \xi_t\} \subset \Omega$ be a set of sample locations. We denote by $S(f, \xi)$ a sample vector (or a discrete image) of a function (or a continuous scene) $f \in \mathcal{C}(\Omega)$ on ξ , i.e., $S(f, \xi) = (f(\xi_1), f(\xi_2), \dots, f(\xi_t))^\top$. We denote Π_m as the collection of all polynomials in d variables of coordinate-wise degree no more than m . For error analysis, we require the modulus of continuity of $f \in \mathcal{C}(\Omega)$, which is given by

$$\omega_f(r; \Omega) := \sup_{\substack{x_1, x_2 \in \Omega, \\ \|x_1 - x_2\|_2 \leq r}} |f(x_1) - f(x_2)|. \quad (13)$$

We define $\mathcal{U}(L, K)$ as U-shaped networks that contain no more than L layers and a maximum of K training parameters. The precise definition is provided in the appendix. To derive non-asymptotic error bounds, the following two assumptions are posited.

Assumption 4.1. We assume that the mapping \mathcal{M} satisfies the Lipschitz property, i.e., for any $f_1, f_2 \in \mathcal{C}(\Omega)$, $\|\mathcal{M}(f_1) - \mathcal{M}(f_2)\|_{L_\infty} \leq L_{\mathcal{M}} \|f_1 - f_2\|_{L_\infty}$ for some constant $L_{\mathcal{M}}$.

Assumption 4.2. We assume that any function g in the output space $\mathcal{Y} \subset \mathcal{C}(\Omega)$ satisfies $|g(x_1) - g(x_2)| \leq L_{\mathcal{Y}} \|x_1 - x_2\|_2$, for any $x_1, x_2 \in \Omega$ and some constant $L_{\mathcal{Y}}$.

Then the following theorem characterizes the upper bound for approximating \mathcal{M} by U-shaped neural networks.

Theorem 4.3. Let $d, m, L, K \in \mathbb{N}_+$, $t = (m + 1)^d$ and $\Omega = [-1, 1]^d$. Let $\mathcal{X} \subset \{f \in \mathcal{C}(\Omega) : \|f\|_{L_\infty} \leq 1\}$.

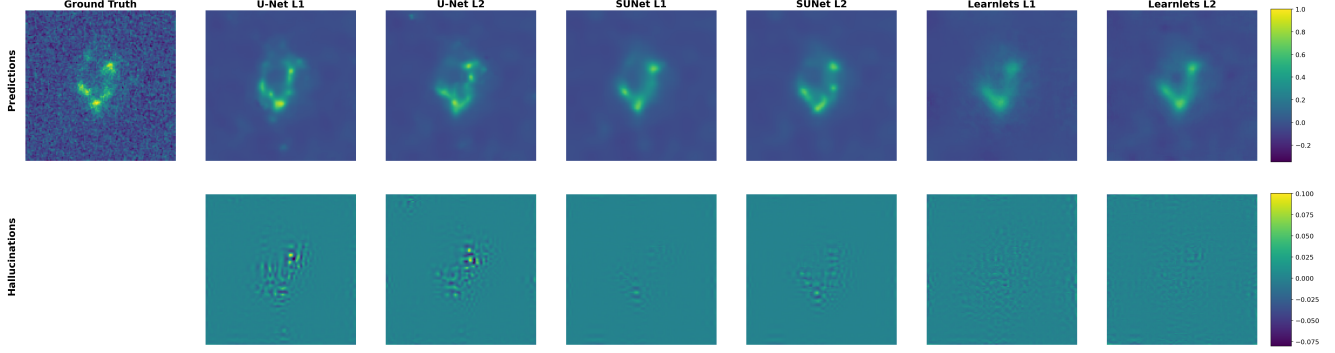


Figure 4. Quantifying hallucinations of U-shaped networks trained with different loss functions using db8. The predicted images are gathered in the first row, while the second row displays CHEM concerning $H^\theta(\Phi)_j$ for high-resolution coefficients relative to j . The U-Net trained with ℓ_2 loss exhibits distinct texture hallucinations, which are identified by CHEM. In contrast, SUNet and Learnlets do not display noticeable hallucinations, consistent with the results in Figures 5, 7, 8. For more information, please see Section 5.

Suppose Assumption 4.1 and Assumption 4.2 hold. Then, there exists a linear mapping $V_m : \mathcal{C}(\Omega) \rightarrow \Pi_m$ and a set of points $\xi_{\text{in}} \subset \Omega$ with $|\xi_{\text{in}}| = t$ such that for any $\xi_{\text{out}} \subset \Omega$ with $|\xi_{\text{out}}| = t$, we can find a U-shaped network $\Phi \in \mathcal{U}(O(L \log(tK)), O(t^2K))$, satisfying

$$\|S(\mathcal{M}(f), \xi_{\text{out}}) - \Phi(S(V_m(f), \xi_{\text{in}}))\|_\infty \quad (14)$$

$$\leq C_1 \omega_f \left(\frac{2}{m} \right) + \frac{C_2}{m} + \frac{C_3 t^3}{(LK \log(K/L))^{1/t}}, \quad (15)$$

for any $f \in \mathcal{X}$. Here, $C_1, C_2, C_3 > 0$ depend on $d, L_{\mathcal{M}}, L_{\mathcal{Y}}$.

In practical scenarios, our estimation must rely on discrete image sets. Consequently, in Theorem 4.3, the input image $X = S(V_m(f), \xi_{\text{in}})$ is discretized from f by using V_m and ξ_{in} , while the true image $Y = S(\mathcal{M}(f), \xi_{\text{out}})$ is considered as a sampled image from $\mathcal{M}(f)$. Each X and Y can be interpreted as a d -dimensional tensor, with each dimension having a size of $m + 1$. Therefore, t denotes the number of elements within X or Y .

The upper bound can be divided into two components. The first component is given by $C_1 \omega_f \left(\frac{2}{m} \right) + \frac{C_2}{m}$. A large value of $\omega_f(\cdot)$ indicates that f lacks smoothness. However, even for highly regular functions, this term cannot be faster than $O(m^{-1})$. Essentially, this component reflects that both the inherent complexity of real scenes and the discretization of f may lead to hallucinations.

The second part, $C_3 t^3 (LK \log(K/L))^{-1/t}$, implies that with a sufficient number of neurons and layers, this component can be made arbitrarily small. However, due to the finite number of image pairs on which neural networks can be trained, there is a risk of overfitting. Additionally, as the dimension d approaches infinity, this term weakens rapidly, indicating that hallucination may occur more often in higher-dimensional scenarios if L and K remain constant. A detailed discussion on Theorem 4.3 is provided in the appendix.

The subsequent theorem supports the previous discussion, as it shows that the lower bound has a similar formula.

Theorem 4.4. Let $d, m \in \mathbb{N}_+$ and $t = (m + 1)^d$. Let $\mathcal{M} : \Pi_m \rightarrow \Pi_m$ and $\mathcal{X} = \Pi_m$. Suppose that Assumption 4.1 holds. Then there exists $\xi_{\text{in}}, \xi_{\text{out}} \subset [-1, 1]^d$ with $|\xi_{\text{in}}| = |\xi_{\text{out}}| = t$ and a constant $C > 0$ such that

$$\inf_{\Phi \in \mathcal{U}(L, K)} \sup_{f \in \mathcal{X}} \|S(\mathcal{M}(f), \xi_{\text{out}}) - \Phi(S(f, \xi_{\text{in}}))\|_\infty \geq C(tK^2 L \log(tK^2))^{-1/t}. \quad (16)$$

5 Experiments

In our experiments, we evaluate the CHEM on different models on astronomical image deconvolution. Specifically, we (i) study the behavior of U-shaped architectures under perturbed inputs, (ii) compare different dictionaries for hallucination quantification, and (iii) analyze the relationship between hallucination and performance during training. The goal is to visually confirm that the metric detects false structures, as shown in [8, 58], and to test the hypothesized tradeoff between performance and hallucination reported in [17, 58].

5.1 Deep learning in image deconvolution

Image deconvolution: Advances in information processing have expanded the possibilities of astronomical imaging, making robust image processing techniques increasingly important. Hybrid approaches that combine deep learning with classical techniques [55] are of particular interest. Here, we experimentally analyze the hallucinations produced by such methods in the context of reconstructing high-quality ground-based all-sky images. This setting naturally leads to an image deconvolution problem, i.e. the task of recovering a ground truth image x from an observed

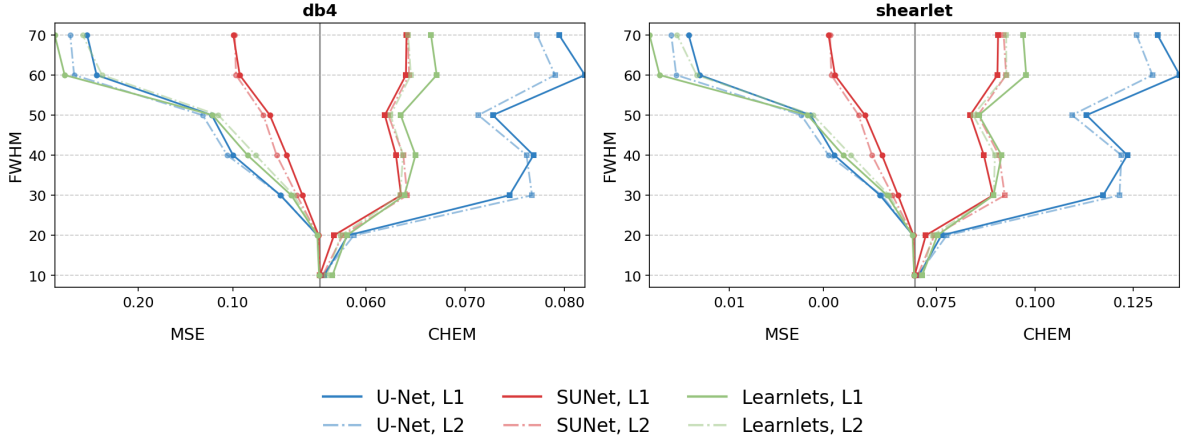


Figure 5. MSE/CHEM-FWHM curves under different dictionaries. This figure illustrates the effect of the chosen representation.

image y , modeled as $y = h * x + \eta$, where h is the point spread function (PSF), η represents additive Gaussian noise, and $*$ denotes the 2D convolution operation. Figure 6 illustrates the image deconvolution problem on the CANDELS dataset.

Two-stage deep deconvolution methods: We analyze the hallucination behavior of a two-stage deep deconvolution method for astronomical images [2]. This method

$$y = h * x + \eta$$

Figure 6. Image deconvolution task on the CANDELS dataset.

combines a deconvolution step followed by a neural network-based denoising stage. The motivation behind this is to combine the stability and interpretability of classical regularized deconvolution with the representation power of deep neural networks, leading to improved reconstruction accuracy [1, 47, 55].

U-shaped networks for evaluation: To evaluate the influence of network architectures, we consider three alternatives for the denoising stage: U-Net [55], Learnlets [47] and the Swin Transformer U-Net (SUNet) [2]. As summarized in Table 1, these configurations correspond to large, medium, and lightweight models, chosen to assess hallucination effects across different model capacities. For a detailed description of the architectures, we refer to the Appendix.

5.2 Dataset, training setting, and evaluation

CANDELS dataset: This study is based on images from the Cosmic Assembly Near-IR Deep Extragalactic Legacy

Survey (CANDELS) [18, 27]. The dataset contains images of more than 250000 galaxies. Data extraction was performed following the procedure described in [1]. This resulted in an initial dataset of 20 085 samples. From this dataset, we used 10000 cutouts for training, of which 70% were employed for training and 30% for validation in each epoch. The calibration dataset used for the computation of the CHEM consists of the remaining samples from the initial dataset, which were evenly divided into \mathcal{D}_1 for initializing $\hat{r}(\cdot)$ (e.g., see [48, Section 3]) and \mathcal{D}_2 for calculating $\hat{R}(\cdot)$. We set $\alpha = 0.01$ and $\theta = 1$. We evaluate our methods on a test set comprising 2 232 galaxies.

Training setting: In order to enable a fair comparison across architectures, we trained all networks using the same set of parameters. The only variation across experiments was the choice of loss function, where we considered either ℓ_1 or ℓ_2 loss depending on the configuration. The network weights corresponding to the epoch with the highest validation Peak Signal-to-Noise Ratio (PSNR) were saved and used for all subsequent analysis.

Method	Loss	No. of parameters	Batch size	Epochs	Training Time [h]
Learnlets	L1	21,673	4	500	65.9
Learnlets	L2	21,673	4	500	61.0
SUNet	L1	99,475,367	4	500	134.0
SUNet	L2	99,475,367	4	500	135.1
U-Net	L1	7,781,761	4	500	75.0
U-Net	L2	7,781,761	4	500	76.4

Table 1. Training configurations.

Evaluation details: Figures 3 and 4 visually motivate the subsequent analysis, illustrating that our definition effectively captures the plausible yet inconsistent textures that characterize hallucinations in image reconstruction. To ensure comparability across experiments, all shearlet coefficients were normalized by the root-mean-square (RMS)

value of their respective subband. For Figures 3 and 4, the CHEM values for each coefficient j in an image were further normalized as $(H^\theta(\Phi)_j - \bar{H}^\theta(\Phi)) / \sigma_{H^\theta(\Phi)_j}$, where $H^\theta(\Phi)$ and $\sigma_{H^\theta(\Phi)_j}$ denote the mean and standard deviation of the hallucination values, respectively. We then selected fine-scale coefficients with values above 0.5 and reconstructed these.

5.3 Hallucination under input perturbations

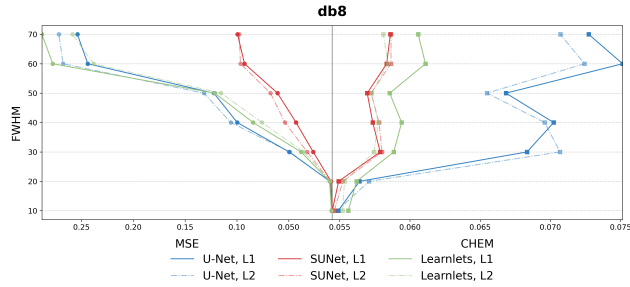


Figure 7. MSE/CHEM-FWHM curves. We analyze the changes in MSE/CHEM with varying FWHM of disturbed inputs to demonstrate the robustness of U-shaped architectures.

Understanding model behavior when provided with perturbed inputs is crucial, since a reliable model should maintain stability. In this experiment, we perturb the inputs by varying the full width at half maximum (FWHM) of the PSF, with details provided in the appendix, and compute the corresponding CHEM for the wavelet coefficients of the image as described in Algorithm 1. Figure 7 illustrates that both SUNet and U-Net achieve a lower performance when employing ℓ_1 loss, and they also exhibit a decrease in the extent of hallucinations with minor perturbations. This suggests that in large neural networks, the application of ℓ_1 loss could be advantageous for enhancing performance while minimizing hallucination levels. On the other hand, Learnlets achieves MSEs similar to those of U-Net under both losses, but its effectiveness in reducing hallucinations is significantly better than that of U-Net. Therefore, in contrast to MSE, CHEM might provide an alternative viewpoint on the model’s behavior. Figure 4 illustrates the quantification of hallucinations using various U-shaped architectures. The U-Net trained with ℓ_2 loss, displays distinct texture hallucinations, which are effectively identified by our CHEM method. Conversely, SUNet and Learnlets do not exhibit noticeable hallucinations in their predicted images, consistent with their corresponding MSE-CHEM/FWHM curves.

5.4 Hallucination under varying dictionaries

To further analyze the impact of the chosen representation, we additionally considered Daubechies-4 (Db4) and shearlets. Figure 5 summarizes the results for these addi-

tional dictionaries. Although some variations can be observed when changing the transformation, the general trend remains consistent with that of Figure 7: Learnlets- and SUNet-based deconvolution methods exhibit greater stability than U-Net under CHEM.

5.5 Hallucination-performance tradeoff

In the last experiment, we compare hallucination with training loss to examine CHEM during training. Figure 8 shows the evolution of hallucination with respect to the corresponding training loss over the first 300 epochs. The metrics are normalized per model using a min–max scaling. The tradeoff between MSE and CHEM is most evident for U-Net: beyond a certain number of epochs, further reductions in training loss come at the cost of increased hallucination. The tradeoff phenomenon of SUNet is also observed after about 40 epochs, albeit with a smaller degree of hallucination compared to U-Net. In contrast, Learnlets exhibits the most stable behavior, maintaining low hallucination levels throughout training. It may, however, approach a tradeoff beyond 300 epochs.

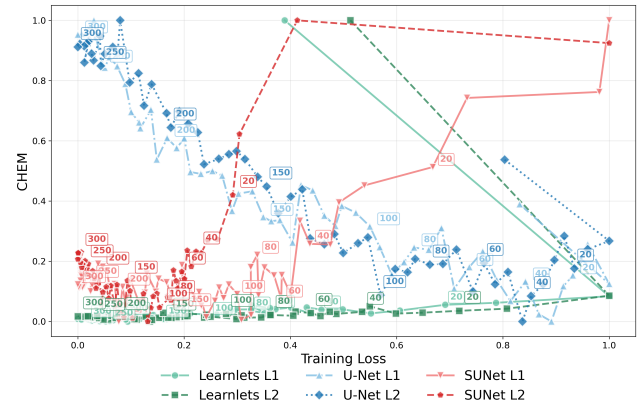


Figure 8. Evolution of the db8-based CHEM and training loss over the first 300 epochs, averaged across all test images. All metrics are normalized per model.

6 Limitations

The proposed approach relies on predefined dictionaries. For images from diverse domains, the selection of a different dictionary might enhance the efficiency of detecting hallucinations. Additionally, our experiments demonstrate that there is a balance between hallucination and performance. In our future research, we plan to refine our method by enabling dictionaries to automatically adjust to the relevant images and to expand the analysis of the causes behind the performance-hallucination tradeoff phenomenon.

7 Conclusion

We introduced a new theoretical framework to quantify and understand hallucinations in imaging. Using conformalized quantile regression, we developed a distribution-free hallucination measure (CHEM) based on wavelet and shearlet representations. Additionally, focusing on U-shaped architectures, we pinpointed various factors that lead to these unrealistic artifacts. Our experiments demonstrate the value and significance of CHEM in identifying and measuring artifacts that MSE does not fully capture. This is particularly crucial in imaging fields, such as medical imaging, where maintaining the consistency of reconstructed images is vital.

Acknowledgement

J. Li gratefully acknowledges support from the project CONFORM, funded by the German Federal Ministry of Education and Research (BMBF), as well as from the German Research Foundation under the Grant DFG-SPP-2298. Furthermore, J. Li acknowledges additional support from the project ‘‘Next Generation AI Computing (gAIn)’’, funded by the Bavarian Ministry of Science and the Arts and the Saxon Ministry for Science, Culture, and Tourism. I. Rosellon-Inclan gratefully acknowledges support from the project CONFORM, funded by the German Federal Ministry of Education and Research (BMBF). The work of G. Kutyniok was supported in part by the Konrad Zuse School of Excellence in Reliable AI (DAAD), the Munich Center for Machine Learning (MCML), as well as the German Research Foundation under Grants DFG-SPP-2298, KU 1446/31-1 and KU 1446/32-1. Furthermore, G. Kutyniok acknowledges additional support from the project ‘‘Next Generation AI Computing (gAIn)’’, funded by the Bavarian Ministry of Science and the Arts and the Saxon Ministry for Science, Culture, and Tourism, as well as by the Hightech Agenda Bavaria. The work of J. Starck was supported by the TITAN ERA Chair project (contract no. 101086741) within the Horizon Europe Framework Programme of the European Commission, and additionally by the Agence Nationale de la Recherche (ANR-22-CE31-0014-01 TOSCA).

References

[1] Utsav Akhaury, Jean-Luc Starck, Pascale Jablonka, Frédéric Courbin, and Kevin Michalewicz. Deep learning-based galaxy image deconvolution. *Frontiers in Astronomy and Space Sciences*, 9, 2022. Publisher: Frontiers.

[2] U. Akhaury, P. Jablonka, J.-L. Starck, and F. Courbin. Ground-based image deconvolution with Swin Transformer UNet. *Astronomy & Astrophysics*, 688:A6, 2024.

[3] Anastasios N Angelopoulos, Amit Pal Kohli, Stephen Bates, Michael Jordan, Jitendra Malik, Thayer Alshaabi, Srigokul Upadhyayula, and Yaniv Romano. Image-to-image regression with distribution-free uncertainty quantification and applications in imaging. In *International Conference on Machine Learning*, pages 717–730. PMLR, 2022.

[4] Harrison H Barrett and Kyle J Myers. *Foundations of Image Science*. John Wiley & Sons, 2013.

[5] Peter L Bartlett, Nick Harvey, Christopher Liaw, and Abbas Mehrabian. Nearly-tight VC-dimension and pseudodimension bounds for piecewise linear neural networks. *Journal of Machine Learning Research*, 20(63):1–17, 2019.

[6] Omer Belhasin, Yaniv Romano, Daniel Freedman, Ehud Rivlin, and Michael Elad. Principal Uncertainty Quantification with Spatial Correlation for Image Restoration Problems, 2024. arXiv:2305.10124 [cs].

[7] Chinmay Belthangady and Loic A. Royer. Applications, promises, and pitfalls of deep learning for fluorescence image reconstruction. *Nature Methods*, 16(12):1215–1225, 2019.

[8] Sayantan Bhadra, Varun A. Kelkar, Frank J. Brooks, and Mark A. Anastasio. On hallucinations in tomographic image reconstruction. *IEEE Transactions on Medical Imaging*, 40(11):3249–3260, 2021.

[9] Hu Cao, Yueyue Wang, Joy Chen, Dongsheng Jiang, Xiaopeng Zhang, Qi Tian, and Manning Wang. Swin-UNet: Unet-like pure transformer for medical image segmentation. In *Computer Vision – ECCV 2022 Workshops*, pages 205–218, 2023.

[10] Jieneng Chen, Yongyi Lu, Qihang Yu, Xiangde Luo, Ehsan Adeli, Yan Wang, Le Lu, Alan L. Yuille, and Yuyin Zhou. TransUNet: Transformers make strong encoders for medical image segmentation, 2021. arXiv:2102.04306 [cs].

[11] Liang-Chieh Chen, Yukun Zhu, George Papandreou, Florian Schroff, and Hartwig Adam. Encoder-decoder with atrous separable convolution for semantic image segmentation. In *Proceedings of the European conference on computer vision (ECCV)*, pages 801–818, 2018.

[12] Regev Cohen, Idan Kligvasser, Ehud Rivlin, and Daniel Freedman. Looks too good to be true: An information-theoretic analysis of hallucinations in generative restoration models. *Advances in Neural Information Processing Systems*, 37:22596–22623, 2024.

[13] Jean Baptiste Cordonnier, Andreas Loukas, and Martin Jaggi. On the relationship between self-attention and convolutional layers. In *8th International Conference on Learning Representations, ICLR 2020*, 2020.

[14] Ingrid Daubechies. *Ten Lectures on Wavelets*. Society for Industrial and Applied Mathematics, 1992.

[15] Philip J Davis. *Interpolation and approximation*. Courier Corporation, 1975.

[16] Chi-Mao Fan, Tsung-Jung Liu, and Kuan-Hsien Liu. SUNet: Swin transformer UNet for image denoising. In *2022 IEEE International Symposium on Circuits and Systems (ISCAS)*, pages 2333–2337. IEEE, 2022.

[17] Nina M. Gottschling, Vegard Antun, Anders C. Hansen, and Ben Adcock. The troublesome kernel: On hallucinations, no free lunches, and the accuracy-stability tradeoff in inverse problems. *SIAM Review*, 67(1):73–104, 2025. Publisher: Society for Industrial and Applied Mathematics.

[18] Norman A. Grogin, Dale D. Kocevski, S. M. Faber, Henry C. Ferguson, Anton M. Koekemoer, Adam G. Riess, Viviana Acquaviva, David M. Alexander, Omar Almaini, Matthew L. N. Ashby, Marco Barden, Eric F. Bell, Frédéric Bournaud, Thomas M. Brown, Karina I. Caputi, Stefano Casertano, Paolo Cassata, Marco Castellano, Peter Challis, Ranga-Ram Chary, Edmond Cheung, Michele Cirasuolo, Christopher J. Conselice, Asantha Roshan Cooray, Darren J. Croton, Emanuele Daddi, Tomas Dahlen, Romeel Davé, Duilia F. de Mello, Avishai Dekel, Mark Dickinson, Timothy Dolch, Jennifer L. Donley, James S. Dunlop, Aaron A. Dutton, David Elbaz, Giovanni G. Fazio, Alexei V. Filippenko, Steven L. Finkelstein, Adriano Fontana, Jonathan P. Gardner, Peter M. Garnavich, Eric Gawiser, Mauro Giavalisco, Andrea Grazian, Yicheng Guo, Nimish P. Hathi, Boris Häussler, Philip F. Hopkins, Jia-Sheng Huang, Kuang-Han Huang, Saurabh W. Jha, Jeyhan S. Kartaltepe, Robert P. Kirshner, David C. Koo, Kamson Lai, Kyoung-Soo Lee, Weidong Li, Jennifer M. Lotz, Ray A. Lucas, Piero Madau, Patrick J. McCarthy, Elizabeth J. McGrath, Daniel H. McIntosh, Ross J. McLure, Bahram Mobasher, Leonidas A. Moustakas, Mark Mozena, Kirpal Nandra, Jeffrey A. Newman, Sami-Matias Niemi, Kai G. Noeske, Casey J. Papovich, Laura Pentericci, Alexandra Pope, Joel R. Primack, Abhijith Rajan, Swara Ravindranath, Naveen A. Reddy, Alvio Renzini, Hans-Walter Rix, Aday R. Robaina, Steven A. Rodney, David J. Rosario, Piero Rosati, Sara Salimbeni, Claudia Scarlata, Brian Siana, Luc Simard, Joseph Smidt, Rachel S. Somerville, Hyron Spinrad, Amber N. Straughn, Louis-Gregory Strolger, Olivia Telford, Harry I. Teplitz, Jonathan R. Trump, Arjen van der Wel, Carolin Villforth, Risa H. Wechsler, Benjamin J. Weiner, Tommy Wiklind, Vivienne Wild, Grant Wilson, Stijn Wuyts, Hao-Jing Yan, and Min S. Yun. CANDELS: The cosmic assembly near-infrared deep extragalactic legacy survey. *The Astrophysical Journal Supplement Series*, 197:35, 2011.

[19] Ingo Gühring, Gitta Kutyniok, and Philipp Petersen. Error bounds for approximations with deep relu neural networks in $w^{s,p}$ norms. *Analysis and Applications*, 18(05):803–859, 2020.

[20] Kanghui Guo, Gitta Kutyniok, and Demetrio Labate. Sparse multidimensional representations using anisotropic dilation and shear operators. *Wavelets and Splines*, 14:189–201, 2006.

[21] Iryna Gurevych, Michael Kohler, and Gözde Gülden. On the rate of convergence of a classifier based on a transformer encoder. *IEEE Transactions on Information Theory*, 68(12):8139–8155, 2022.

[22] Yoseob Han and Jong Chul Ye. Framing U-Net via deep convolutional framelets: Application to sparse-view CT. *IEEE Transactions on Medical Imaging*, 37(6):1418–1429, 2018.

[23] Yunpeng Huang, Jingwei Xu, Junyu Lai, Zixu Jiang, Taolue Chen, Zenan Li, Yuan Yao, Xiaoxing Ma, Lijuan Yang, Hao Chen, Shupeng Li, and Penghao Zhao. Advancing transformer architecture in long-context large language models: A comprehensive survey, 2024. arXiv:2311.12351 [cs].

[24] Fabian Isensee, Paul F. Jaeger, Simon A. A. Kohl, Jens Petersen, and Klaus H. Maier-Hein. nnU-Net: a self-configuring method for deep learning-based biomedical image segmentation. *Nature Methods*, 18(2):203–211, 2021.

[25] Andrew Jesson, Nicolas Beltran-Velez, Quentin Chu, Sweta Karlekar, Jannik Kossen, Yarin Gal, John P Cunningham, and David Blei. Estimating the hallucination rate of generative AI. *Advances in Neural Information Processing Systems*, 37:31154–31201, 2024.

[26] Ziwei Ji, Nayeon Lee, Rita Frieske, Tiezheng Yu, Dan Su, Yan Xu, Etsuko Ishii, Ye Jin Bang, Andrea Madotto, and Pascale Fung. Survey of hallucination in natural language generation. *ACM Computing Surveys*, 55(12):1–38, 2023.

[27] Anton M. Koekemoer, S. M. Faber, Henry C. Ferguson, Norman A. Grogin, Dale D. Kocevski, David C. Koo, Kamson Lai, Jennifer M. Lotz, Ray A. Lucas, Elizabeth J. McGrath, Sara Ogaz, Abhijith Rajan, Adam G. Riess, Steve A. Rodney, Louis Strolger, Stefano Casertano, Marco Castellano, Tomas Dahlen, Mark Dickinson, Timothy Dolch, Adriano Fontana, Mauro Giavalisco, Andrea Grazian, Yicheng Guo, Nimish P. Hathi, Kuang-Han Huang, Arjen van der Wel, Hao-Jing Yan, Viviana Acquaviva, David M. Alexander, Omar Almaini, Matthew L. N. Ashby, Marco Barden, Eric F. Bell, Frédéric Bournaud, Thomas M. Brown, Karina I. Caputi, Paolo Cassata, Peter Challis, Ranga-Ram Chary, Edmond Cheung, Michele Cirasuolo, Christopher J. Conselice, Asantha Roshan Cooray, Darren J. Croton, Emanuele Daddi, Romeel Davé, Duilia F. de Mello, Loic de Ravel, Avishai Dekel, Jennifer L. Donley, James S. Dunlop, Aaron A. Dutton, David Elbaz, Giovanni G. Fazio, Alex V. Filippenko, Steven L. Finkelstein, Chris Frazer, Jonathan P. Gardner, Peter M. Garnavich, Eric Gawiser, Ruth Gruetzbach, Will G. Hartley, Boris Häussler, Jessica Herrington, Philip F. Hopkins, Jia-Sheng Huang, Saurabh Jha, Andrew Johnson, Jeyhan S. Kartaltepe, Ali Ahmad Khostovan, Robert P. Kirshner, Caterina Lani, Kyoung-Soo Lee, Weidong Li, Piero Madau, Patrick J. McCarthy, Daniel H. McIntosh, Ross J. McLure, Conor McPartland, Bahram Mobasher, Heidi Moreira, Allice Mortlock, Leonidas A. Moustakas, Mark Mozena, Kirpal Nandra, Jeffrey A. Newman, Jennifer L. Nielsen, Sami Niemi, Kai G. Noeske, Casey J. Papovich, Laura Pentericci, Alexandra Pope, Joel R. Primack, Swara Ravindranath, Naveen A. Reddy, Alvio Renzini, Hans-Walter Rix, Aday R. Robaina, David J. Rosario, Piero Rosati, Sara Salimbeni, Claudia Scarlata, Brian Siana, Luc Simard, Joseph Smidt, Diana Snyder, Rachel S. Somerville, Hyron Spinrad, Amber N. Straughn, Olivia Telford, Harry I. Teplitz, Jonathan R. Trump, Carlos Vargas, Carolin Villforth, Cory R. Wagner, Pat Wandro, Risa H. Wechsler, Benjamin J. Weiner, Tommy Wiklind, Vivienne Wild, Grant Wilson, Stijn Wuyts, and Min S. Yun. CANDELS: The cosmic assembly near-infrared deep extragalactic legacy survey - the hubble space telescope observations, imaging data products and mosaics. *The Astrophysical Journal Supplement Series*, 197(2):36, 2011. arXiv:1105.3754 [astro-ph].

[28] Stefan Kolek, Robert Windesheim, Hector Andrade-Loarca, Gitta Kutyniok, and Ron Levie. Explaining image classifiers with multiscale directional image representation. In *Proceedings of the IEEE/CVF Conference on Computer Vision and Pattern Recognition*, pages 18600–18609, 2023.

[29] Rajeev Ranjan Kumar, S Vishnu Shankar, Ronit Jaiswal, Mrinmoy Ray, Neeraj Budhlakoti, and KN Singh. Advances in deep learning for medical image analysis: A comprehensive investigation. *Journal of Statistical Theory and Practice*, 19(1):9, 2025.

[30] Gilad Kutiel, Regev Cohen, Michael Elad, Daniel Freedman, and Ehud Rivlin. Conformal prediction masks: Visualizing uncertainty in medical imaging. In *Trustworthy Machine Learning for Healthcare*, pages 163–176, 2023.

[31] Gitta Kutyniok and Demetrio Labate. *Shearlets: Multiscale analysis for multivariate data*. Springer Science & Business Media, 2012.

[32] Gitta Kutyniok, Wang-Q Lim, and Rafael Reisenhofer. Shearlab 3D: Faithful digital shearlet transforms based on compactly supported shearlets. *ACM Transactions on Mathematical Software (TOMS)*, 42(1):1–42, 2016.

[33] Hubert Leterme, Jalal Fadili, and J-L Starck. Distribution-free uncertainty quantification for inverse problems: Application to weak lensing mass mapping. *Astronomy & Astrophysics*, 694:A267, 2025.

[34] Jianfei Li, Han Feng, and Xiaosheng Zhuang. Convolutional neural networks for spherical signal processing via area-regular spherical haar tight framelets. *IEEE Transactions on Neural Networks and Learning Systems*, 35(4):4400–4410, 2022.

[35] Jianfei Li, Han Feng, and Ding-Xuan Zhou. Approximation analysis of CNNs from a feature extraction view. *Analysis and Applications*, 22(03):635–654, 2024.

[36] Hanchao Liu, Wenyuan Xue, Yifei Chen, Dapeng Chen, Xiutian Zhao, Ke Wang, Liping Hou, Rongjun Li, and Wei Peng. A survey on hallucination in large vision-language models, 2024. arXiv:2402.00253 [cs].

[37] Pengju Liu, Hongzhi Zhang, Kai Zhang, Liang Lin, and Wangmeng Zuo. Multi-level wavelet-CNN for image restoration. In *Proceedings of the IEEE conference on computer vision and pattern recognition workshops*, pages 773–782, 2018.

[38] Ze Liu, Yutong Lin, Yue Cao, Han Hu, Yixuan Wei, Zheng Zhang, Stephen Lin, and Baining Guo. Swin transformer: Hierarchical vision transformer using shifted windows. In *2021 IEEE/CVF International Conference on Computer Vision (ICCV)*, pages 9992–10002, 2021.

[39] Jun Ma, Feifei Li, and Bo Wang. U-Mamba: Enhancing long-range dependency for biomedical image segmentation, 2024. arXiv:2401.04722 [eess].

[40] Stéphane Mallat. *A Wavelet Tour of Signal Processing*. Elsevier, 1999.

[41] Ambuj Mehrish, Navonil Majumder, Rishabh Bharadwaj, Rada Mihalcea, and Soujanya Poria. A review of deep learning techniques for speech processing. *Information Fusion*, 99:101869, 2023.

[42] Song Mei. U-Nets as belief propagation: Efficient classification, denoising, and diffusion in generative hierarchical models, 2024. arXiv:2404.18444 [cs].

[43] Hrushikesh Narhar Mhaskar and Nahmwoo Hahm. Neural networks for functional approximation and system identification. *Neural Computation*, 9(1):143–159, 1997.

[44] Matthew J. Muckley, Bruno Riemenschneider, Alireza Radmanesh, Sunwoo Kim, Geunu Jeong, Jingyu Ko, Yohan Jun, Hyungseob Shin, Dosik Hwang, Mahmoud Mostapha, Simon Arberet, Dominik Nickel, Zaccharie Ramzi, Philippe Ciuciu, Jean-Luc Starck, Jonas Teuwen, Dimitrios Karkalousos, Chaoping Zhang, Anuroop Sriram, Zhengnan Huang, Nafissa Yakubova, Yvonne W. Lui, and Florian Knoll. Results of the 2020 fastMRI challenge for machine learning MR image reconstruction. *IEEE Transactions on Medical Imaging*, 40(9):2306–2317, 2021.

[45] Ozan Oktay, Jo Schlemper, Loic Le Folgoc, Matthew Lee, Matthias Heinrich, Kazunari Misawa, Kensaku Mori, Steven McDonagh, Nils Y. Hammerla, Bernhard Kainz, Ben Glocker, and Daniel Rueckert. Attention U-Net: Learning where to look for the pancreas, 2018. arXiv:1804.03999 [cs].

[46] Xuebin Qin, Zichen Zhang, Chenyang Huang, Masood Dehghan, Osmar R Zaiane, and Martin Jagersand. U2-Net: Going deeper with nested U-structure for salient object detection. *Pattern recognition*, 106:107404, 2020.

[47] Zaccharie Ramzi, Kevin Michalewicz, Jean-Luc Starck, Thomas Moreau, and Philippe Ciuciu. Wavelets in the deep learning era. *Journal of Mathematical Imaging and Vision*, 65(1):240–251, 2023.

[48] Yaniv Romano, Evan Patterson, and Emmanuel Candes. Conformalized quantile regression. *Advances in Neural Information Processing Systems*, 32, 2019.

[49] Olaf Ronneberger, Philipp Fischer, and Thomas Brox. U-Net: Convolutional networks for biomedical image segmentation. In *International Conference on Medical Image Computing and Computer-Assisted Intervention*, pages 234–241. Springer, 2015.

[50] Pranab Sahoo, Prabhush Meharia, Akash Ghosh, Sriparna Saha, Vinija Jain, and Aman Chadha. A comprehensive survey of hallucination in large language, image, video and audio foundation models, 2024. arXiv:2405.09589 [cs].

[51] Swami Sankaranarayanan, Anastasios N. Angelopoulos, Stephen Bates, Yaniv Romano, and Phillip Isola. Semantic uncertainty intervals for disentangled latent spaces, 2022. arXiv:2207.10074 [cs].

[52] Martin H Schultz. L^∞ -multivariate approximation theory. *SIAM Journal on Numerical Analysis*, 6(2):161–183, 1969.

[53] Zuowei Shen, Haizhao Yang, and Shijun Zhang. Optimal approximation rate of ReLU networks in terms of width and depth. *Journal de Mathématiques Pures et Appliquées*, 157:101–135, 2022.

[54] J.-L. Starck and F. Murtagh. *Astronomical Image and Data Analysis*. Springer, 2006.

[55] Florent Sureau, Alexis Lechat, and J-L Starck. Deep learning for a space-variant deconvolution in galaxy surveys. *Astronomy & Astrophysics*, 641:A67, 2020.

[56] Xue-Cheng TAI, Hao LIU, Raymond H CHAN, and Lingfeng LI. A mathematical explanation of UNet. *Mathematical Foundations of Computing*, 8(5):874–889, 2025.

[57] Jacopo Teneggi, J Webster Stayman, and Jeremias Sulam. Conformal risk control for semantic uncertainty quantification in computed tomography. In *International Conference on Medical Image Computing and Computer-Assisted Intervention*, pages 45–55, 2025.

[58] Matthew Tivnan, Siyeop Yoon, Zhenhong Chen, Xiang Li, Dufan Wu, and Quanzheng Li. Hallucination index: An image quality metric for generative reconstruction models. In *International Conference on Medical Image Computing and Computer-Assisted Intervention*, pages 449–458. Springer, 2024.

[59] Christopher Williams, Fabian Falck, George Deligiannidis, Chris C Holmes, Arnaud Doucet, and Saifuddin Syed. A unified framework for U-Net design and analysis. *Advances in Neural Information Processing Systems*, 36:27745–27782, 2023.

[60] Yunfei Yang. On the optimal approximation of Sobolev and Besov functions using deep ReLU neural networks. *Applied and Computational Harmonic Analysis*, page 101797, 2025.

[61] Yue Zhang, Yafu Li, Leyang Cui, Deng Cai, Lemao Liu, Tingchen Fu, Xinting Huang, Enbo Zhao, Yu Zhang, Yulong Chen, Longyue Wang, Anh Tuan Luu, Wei Bi, Freda Shi, and Shuming Shi. Siren’s song in the ai ocean: A survey on hallucination in large language models. *Computational Linguistics*, pages 1–46, 2025.

[62] Zhengxin Zhang, Qingjie Liu, and Yunhong Wang. Road extraction by deep residual U-Net. *IEEE Geoscience and Remote Sensing Letters*, 15(5):749–753, 2018.

[63] Zongwei Zhou, Md Mahfuzur Rahman Siddiquee, Nima Tajbakhsh, and Jianming Liang. Unet++: A nested U-Net architecture for medical image segmentation. In *International Workshop on Deep Learning in Medical Image Analysis*, pages 3–11, 2018.

Appendix

The appendix provides additional explanations regarding the experimental setup and the theoretical results. It is structured as follows: Section A covers the essential background on wavelets and shearlets. Section B describes the image-perturbation procedures, the training configuration, and the details of the CHEM visualization. Section C presents the proofs of our theoretical findings. For analyzing U-shaped networks, our approach is simplified by focusing solely on convolutional layers. For other elements like skip connections, self-attention layers, and transformer building blocks of U-shaped networks, we offer a comprehensive discussion and demonstrate that our results could be extended to U-shaped networks that incorporate these popular components.

A Wavelets and Shearlets

In classical signal processing, wavelets have proven to be an efficient tool for extracting image textures [40]. For an image modeled as a function f in $L_2(\mathbb{R}^2)$, we can use an orthonormal basis $\{\psi_{j,n}^k, k = 1, 2, 3\}_{(j,n) \in \mathbb{Z}^2}$ for analyzing texture information. Here, $\psi_{j,n}^k$ forms the wavelet family, which is generated by some wavelets $\psi^k, k = 1, 2, 3$ and is

given by

$$\psi_{j,n}^k(x) = \frac{1}{2^j} \psi^k \left(\frac{x_1 - 2^j n_1}{2^j}, \frac{x_2 - 2^j n_2}{2^j} \right).$$

This yields information at different scales 2^j . Then, the wavelet representation decomposes f into

$$f = \sum_{(j,n) \in \mathbb{Z}^2} \sum_{k=1}^3 \langle f, \psi_{j,n}^k \rangle \psi_{j,n}^k.$$

The coefficient $\langle f, \psi_{j,n}^k \rangle$ in this decomposition contains vertical, horizontal, and diagonal texture information of f for different $k \in \{1, 2, 3\}$. As a result, under wavelet decomposition, we can consider texture-level contents of different directions instead of analyzing every pixel independently. For the theoretical analysis and discrete transformation algorithms we refer to [40].

The shearlet system is an improvement of the wavelet system for efficient anisotropic feature extraction. Let

$$M_{as} := \begin{pmatrix} a & s\sqrt{a} \\ 0 & \sqrt{a} \end{pmatrix}.$$

Then, a shearlet system is defined as the collection $\{\psi_{ast}(x) = a^{-3/4} \psi(M_{as}^{-1}(x - t)) : a \in \mathbb{R}_+, s \in \mathbb{R}, t \in \mathbb{R}^2\}$ for some ψ . And for any $f \in L_2(\mathbb{R}^2)$, we have

$$\|f\|_{L_2(\mathbb{R}^2)}^2 = \int_{\mathbb{R}^2} \int_{\mathbb{R}} \int_0^\infty |\langle f, \psi_{ast} \rangle|^2 \frac{da}{a} ds dt.$$

The studies [20, 31, 32] provide a thorough discussion of theoretical insights and the discrete shearlet transform.

B Experimental Details

B.1 Input perturbation

In the deconvolution problem, the point spread functions PSF is assumed to be known. In real applications, the PSF needs to be reconstructed and the use of different instruments for measurements can result in variations of the PSF [54]. In our setting, we simulate these differences by convolving the ground truth images with a normalized Gaussian PSF of varying full width at half maximum (FWHM). For an image of size $n \times n$, we index pixel positions by (k, l) with $1 \leq k, l \leq n$, and define the center of the kernel as $(k_0, l_0) = (\frac{n+1}{2}, \frac{n+1}{2})$. The PSF is then given by

$$g_{k,l} = \frac{\exp\left(-\frac{(k-k_0)^2 + (l-l_0)^2}{2\sigma^2}\right)}{\sum_{k,l=1}^n \exp\left(-\frac{(k-k_0)^2 + (l-l_0)^2}{2\sigma^2}\right)},$$

where $\text{FWHM} = 2\sqrt{2\ln 2}\sigma$. The larger FWHM values correspond to stronger blurring, whereas the smaller FWHM values indicate sharper imaging performance.

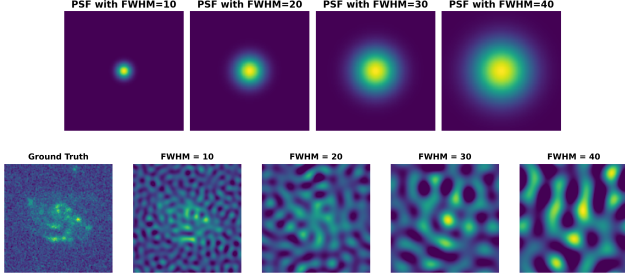


Figure 9. Point spread functions (PSFs) with varying FWHM values and the corresponding ground-truth image after convolution with each PSF.

B.2 Training Configuration

Data extraction is done following the procedure described in [1]. During training, we generate cutouts convolved with a Gaussian PSF of $\text{FWHM} = 15$ and add white Gaussian noise η with a standard deviation σ_{noise} , such that the faintest object in the dataset has a peak signal-to-noise ratio (S/N) close to 1 and is barely visible. The inputs are normalized to the range $[-1, 1]$, and the data is augmented through random rotations, translations, and flips.

Each model is trained for 500 epochs with a batch size of 4. The learning rate is adjusted using a two-stage scheduling strategy that combines a linear warm-up and cosine annealing. During the first three epochs, the learning rate gradually increases from zero to the initial value of 2×10^{-4} (warm-up phase). Subsequently, a cosine annealing scheduler progressively reduces the learning rate to a minimum value of 1×10^{-6} over the remaining training epochs.

Neural network architectures: Learnlets was introduced in 2022 with the aim of preserving the reconstruction and generalization properties of sparsity based approaches, while using the power of neural networks for learning and fast computation. Concretely, it follows the general encoder-decoder principle of U-Net but replaces its design with an analysis-synthesis framework based on learned filter banks. The analysis stage can be interpreted as a wavelet transform with learned filters, while the synthesis stage corresponds to a wavelet reconstruction operator with learned filters. The architecture was originally proposed for denoising and was shown to have better generalization properties than U-Net [47].

Transformers have been highly successful in natural language processing [23]. Their integration into vision tasks initially faced significant challenges but was ultimately achieved with the introduction of Swin Transformers, which substantially reduce the number of parameters through a shifted-window mechanism [38]. A subsequent work of incorporated Swin Transformer blocks into the U-Net architecture, as illustrated in Figure 10, and demonstrated that

this design achieved performance competitive with existing benchmarks in image denoising [16].

Two-stage deep deconvolution method: *Tikhonet* is a two-step deconvolution method [55]. The first step applies Tikhonov deconvolution, followed by a neural network-based denoising step. Recent works apply a variety of architectures for the denoising step, such as the U-Net-based approach [55], the Learnlet-based method [1], and the Swin Transformer U-Net [2].

Tikhonov deconvolution uses a quadratic-regularized inverse filter. Let H denote the circulant matrix associated with the convolution operator h . Then, the deconvolution problem $y = h * x + \eta$ is solved via

$$\hat{x} = (H^\top H + \lambda \Gamma^\top \Gamma)^{-1} H^\top y,$$

where Γ is a linear Tikhonov filter, typically chosen as a Laplacian high-pass filter to penalize high-frequency components, and $\lambda \in \mathbb{R}_+$ is a regularization parameter selected by minimizing Stein’s Unbiased Risk Estimate (SURE). For more details refer to [1].

B.3 Visualization of CHEM

To highlight regions of high uncertainty, as shown in Figure 4, we proceed as follows. Using the notation of Section 3.2, for a data pair (X, Y) and a model Φ . We compute the CHEM $H^\theta(X, Y)_j$ of each coefficient j and normalize $\tilde{H}_j := \frac{H^\theta(\Phi)_j - H^\theta(\Phi)}{\sigma_{H^\theta(\Phi)}}$, where $H^\theta(\Phi)$ and $\sigma_{H^\theta(\Phi)_j}$ denote the mean and standard deviation, respectively. We then retain only those coefficients satisfying $\tilde{H}_j > 0.5$ and lying in the two finest scales, setting all others to zero. Finally, we reconstruct the image from the filtered coefficients. Shearlets offer a similar multiscale decomposition and can be incorporated in an analogous manner; see [31].

Empirically, restricting the reconstruction to the two finest scales yields the sharpest localization of hallucinations. Figure 11 illustrates what happens when all resolutions are included: the resulting maps become diffuse and no longer localize hallucination artifacts as effectively.

A related line of work that leverages conformal prediction to quantify uncertainty for stochastic generative solvers of inverse problems emphasizes the importance of modeling spatial correlations between pixels. Their method constructs a data-driven basis by applying principal component analysis to posterior samples generated by a diffusion model [6]. Another work incorporates semantic information by assessing uncertainty directly in the latent space learned by a generative adversarial network (GAN) [51]. While both approaches capture spatial structure, they cannot exploit the multiscale analysis made possible by wavelets and shearlets, which is particularly important in the study of astronomical data [54].

Tikhonov Deconvolution

U-shaped network denoising

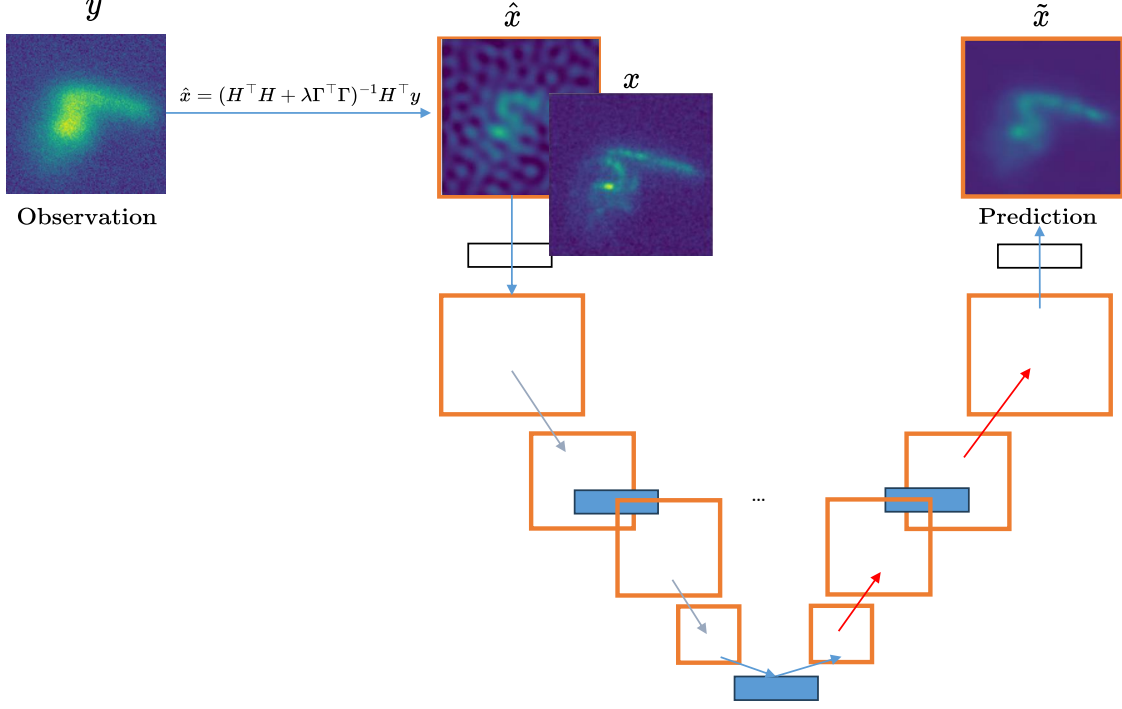


Figure 10. Example: Tikhononet with a U-shaped denoising module. For SUNet, blue filled rectangles indicate Swin-Transformer blocks, red arrows denote dual up-sampling, blue arrows denote patch-merging, and black outlined rectangles correspond to 3×3 convolutions.

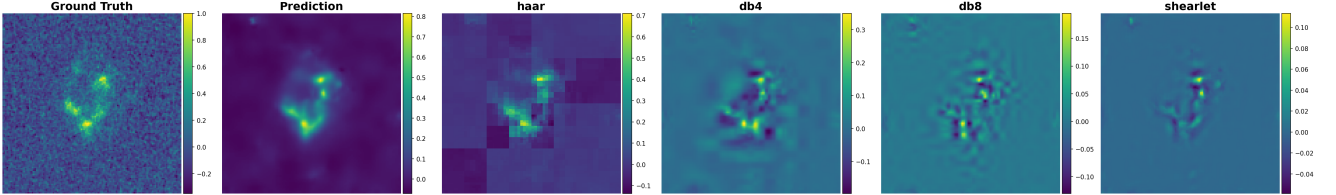


Figure 11. Reproduction of the analysis in Figure 4, now including coarse-scale coefficients. Incorporating all coefficients produces broader, less localized hallucination maps.

C Theoretical Proofs

C.1 Proof of Proposition 3.3

Proof of Proposition 3.3. Let

$$S_M = \sum_{m=1}^M H^\theta(X_m, Y_m)_j.$$

Since $0 \leq H^\theta(X, Y)_j \leq \theta$, Hoeffding's inequality implies that

$$\mathbb{P}(|S_M - \mathbb{E}S_M| \geq t) \leq 2 \exp \left\{ -\frac{2t^2}{M\theta^2} \right\}.$$

Substituting $s = t/M$ into the above inequality, we further have

$$\mathbb{P} \left(\left| \frac{1}{M} S_M - \mathbb{E} \left[\frac{1}{M} S_M \right] \right| \geq s \right) \leq 2 \exp \left\{ -\frac{2Ms^2}{\theta^2} \right\}.$$

Let $s = \sqrt{\frac{\theta^2 \log(2/\delta)}{2M}}$. Notice that $\mathbb{E} \left[\frac{1}{M} S_M \right] = \mathbb{E} H^\theta(X, Y)_j = H^\theta(\Phi)_j$. Hence we finally obtain

$$\mathbb{P} \left(\left| \frac{1}{M} S_M - \mathbb{E} \left[\frac{1}{M} S_M \right] \right| \geq \sqrt{\frac{\theta^2 \log(2/\delta)}{2M}} \right) \leq \delta.$$

The proof is completed by applying similar steps for $H^\theta(\Phi)$. \square

C.2 Notations

We denote $\|\cdot\|_p$, $p \in [1, \infty]$ as the vector norm. Let $\Omega \subset \mathbb{R}^d$ be a compact set. The $L_p(\Omega)$ space contains measurable functions that have a finite L_p norm $\|f\|_{L_p(\Omega)} = (\int_{\Omega} |f(x)|^p dx)^{1/p} < \infty$. For $p = \infty$, we define $\|f\|_{L_{\infty}(\Omega)} := \text{ess sup } |f|$.

Since $L_2(\Omega)$ is a Hilbert space, we denote its inner product as $\langle f_1, f_2 \rangle := \int_{\Omega} f_1(x) f_2(x) dx$. Throughout our proofs, we usually use $\Omega = [-1, 1]^d$ and, for simplicity, write $\|\cdot\|_{L_p} := \|\cdot\|_{L_p(\Omega)}$. We consider $\mathcal{X}, \mathcal{Y} \subset L_2(\Omega)$ are compact sets of $L_2(\Omega)$. The modulus of continuity of a general continuous mapping $\mathcal{M} : L_{\infty}([-1, 1]^d) \rightarrow L_{\infty}([-1, 1]^d)$ is defined as

$$\omega_{\mathcal{M}}(r) := \sup_{\substack{f_1, f_2 \in L_2([-1, 1]^d), \\ \|f_1 - f_2\|_{L_{\infty}} \leq r}} \|\mathcal{M}(f_1) - \mathcal{M}(f_2)\|_{L_{\infty}}.$$

C.3 U-shaped architectures

U-Net represents an architecture of convolutional neural networks primarily designed to solve image segmentation tasks. One way to improve the performance of U-shaped architectures is to add a bottleneck between the encoding path and the decoding path [9, 10, 34, 63]. The bottleneck is used to learn nonlinear transformations of the encoder's deepest features before passing them to the decoder. U-Net corresponds to the special case where the bottleneck is the identity mapping.

C.4 Formal definition of U-shaped networks

For a 1D convolution with a kernel $w \in \mathbb{R}^s$ and a stride t , the convolution operation for $x \in \mathbb{R}^d$ is defined as $(w *_t x)_i = \sum_{k=1}^s w_k x_{(i-1)t+k}$, $i = [\mathcal{D}(d, t)]$, where $\mathcal{D}(d, t) := \lceil d/t \rceil$ and we set $x_i = 0$ for $i > d$. Obviously, there exists a matrix $T^{w, t} \in \mathbb{R}^{\mathcal{D}(d, t) \times d}$ determined by the kernel w and the stride t such that $T^{w, t} x = w *_t x$. Subsequently, we describe a convolutional block consisting of layers L as $\Phi = \mathcal{T}_L \circ \sigma \circ \mathcal{T}_{L-1} \circ \dots \circ \sigma \circ \mathcal{T}_1$, where $\mathcal{T}_{\ell}(z) := T^{w_{\ell}, t_{\ell}} z + b_{\ell}$, $\ell \in [L]$ is associated with a kernel w_{ℓ} , a stride t_{ℓ} , and a bias b_{ℓ} . We use K to denote the total number of parameters in all kernels and bias. In our theoretical analysis, we focus mainly on 1D convolutional blocks. It is important to note that in certain situations, convolutional blocks for processing 2D or higher dimensional tensors, which are more commonly used in image processing tasks, can be simplified into 1D cases [35].

Before defining U-shaped networks, we first introduce multichannel convolutional blocks.

Definition C.1 (Multichannel Convolutional Blocks). *Given an input $x \in \mathbb{R}^d$, a J layer multi-channel CNN block $\phi : \mathbb{R}^d \rightarrow \mathbb{R}^{d_J \times n_J}$ with filters $\{w_{\ell, i}^{(j)} \in \mathbb{R}^{s_j}\}_{j=1}^J$, filter size $\{s_j \geq 2\}_{j=1}^J$, stride $\{t_j \geq 1\}_{j=1}^J$ and channel*

$\{n_j \geq 1\}_{j=1}^J$, is defined iteratively by

$$\begin{aligned} \phi^{(1)}(x)_{\ell} &= \sigma \left(w_{\ell, 1}^{(1)} *_{t_1} x + b_{\ell}^{(1)} \mathbf{1}_{d_1} \right), \ell \in [n_1], \\ \phi^{(j)}(x)_{\ell} &= \sigma \left(\sum_{i=1}^{n_{j-1}} w_{\ell, i}^{(j)} *_{t_j} \phi^{(j-1)}(x)_i + b_{\ell}^{(j)} \mathbf{1}_{d_j} \right), \ell \in [n_j], \\ \phi(x)_{\ell} &= \sum_{i=1}^{n_J} w_{\ell, i}^{(J)} *_{t_J} \phi^{(J-1)}(x)_i + b_{\ell}^{(J)} \mathbf{1}_{d_J}, \ell \in [n_J], \end{aligned}$$

where $b_{\ell}^{(j)} \in \mathbb{R}$ are biases and $d_j = \mathcal{D}(d_{j-1}, t_j)$.

Definition C.2 (U-shaped networks). *A U-shaped network is defined as the composition of an encoding path Φ_{in} , a bottleneck Φ_{bot} , and a decoding path Φ_{out} where Φ_{in} , Φ_{bot} , and Φ_{out} are multichannel convolutional blocks. The summation of layers of all the multichannel convolutional blocks is called the depth/layers of the U-shaped networks, and similarly the summation of number of parameters of all the multichannel convolutional blocks is called the total number of parameters of the U-shaped networks. We denote $\mathcal{U}(L, K)$ as the collection of all U-shaped networks with layers no more than L and the total number of parameters at most K .*

For theoretical ease, the outputs of convolutional blocks which are 1D in each channel are flattened into a vector and serve as the inputs to the subsequent blocks. To prove the main results, we also restrict convolutions for defining $\mathcal{U}(L, K)$ to the case of $s_j = t_j = 2$ for all convolution operations. Other convolutional settings are discussed in [35].

Remark C.3. *Skip connections in U-shaped networks:* In our definition, we did not consider skip connections, which are also a crucial component of U-Net. This omission is due to the fact that [19] demonstrates that any fully connected neural network with skip connections can be equivalently represented by a counterpart lacking skip connections. Therefore, our findings are applicable to U-shaped networks that include skip connections.

Remark C.4. *U-shaped networks constructed with self-attention layers and transformers:* Self-attention mechanisms and transformers have emerged as pivotal elements in deep learning-based image processing models. As illustrated by [13], self-attention mechanisms are capable of approximating any convolution operation. The transformer, which is fundamentally composed of fully connected layers and self-attention, further emphasizes this adaptability, since [35] indicates that convolutional neural networks can represent any fully connected layers. These insights imply that our main results may also extend to U-shaped networks constructed using transformers or self-attention layers.

C.5 Proof of Theorem 4.3

We start with the lemma below, which demonstrates that any continuous function can be closely approximated by a polynomial.

Lemma C.5. *Let $f \in \mathcal{C}([-1, 1]^d)$. There exists a linear operator $V_m : \mathcal{C}([-1, 1]^d) \rightarrow \Pi_m$ such that*

$$\|f - V_m f\|_{L_\infty([-1, 1]^d)} \leq \frac{5d}{4} \omega_f \left(\frac{2}{m}; [-1, 1]^d \right).$$

In addition, we have $\|V_m\|_{L_\infty([-1, 1]^d)} = 1$.

Proof. Let $z = 2x - 1$ where $x \in [0, 1]^d$. We denote $g(x) = f(2x - 1)$. Then the function g is a continuous function in $\mathcal{C}([0, 1]^d)$ and there exists a linear operator $V_m : \mathcal{C}([0, 1]^d) \rightarrow \Pi_m$, defined as

$$\begin{aligned} V_m(g)(x) &:= \sum_{k_1=0}^m \cdots \sum_{k_d=0}^m \binom{m}{k_1} \cdots \binom{m}{k_d} g\left(\frac{k_1}{m}, \dots, \frac{k_d}{m}\right) \\ &\quad \times \prod_{i=1}^d \left(x_i^{k_i} (1 - x_i)^{m-k_i} \right), \end{aligned}$$

such that [52, Theorem 3.1]

$$|g(x) - V_m(g)(x)| \leq \frac{5d}{4} \omega_g \left(\frac{1}{m}; [0, 1]^d \right), \quad \forall x \in [0, 1]^d.$$

Since $g(x) = f(2x - 1)$ and $z = 2x - 1$, we can rewrite the above bound as

$$|f(z) - \tilde{V}_m(f)(z)| \leq \frac{5d}{4} \omega_g \left(\frac{1}{m}; [0, 1]^d \right), \quad \forall z \in [-1, 1]^d, \quad (17)$$

where

$$\begin{aligned} \tilde{V}_m(f)(z) &= \sum_{k_1=0}^m \cdots \sum_{k_d=0}^m \binom{m}{k_1} \cdots \binom{m}{k_d} \\ &\quad \times f\left(\frac{2k_1 - m}{m}, \dots, \frac{2k_d - m}{m}\right) \\ &\quad \times \prod_{i=1}^d \left(\left(\frac{z_i + 1}{2}\right)^{k_i} \left(\frac{1 - z_i}{2}\right)^{m-k_i} \right). \end{aligned}$$

Using the definition of modulus of continuity, we further have

$$\begin{aligned} &\omega_g \left(\frac{1}{m}; [0, 1]^d \right) \\ &= \left\{ |g(x_1) - g(x_2)| : \|x_1 - x_2\|_2 \leq \frac{1}{m}, x_1, x_2 \in [0, 1]^d \right\} \\ &= \left\{ |f(z_1) - f(z_2)| : \|z_1 - z_2\|_2 \leq \frac{2}{m}, z_1, z_2 \in [-1, 1]^d \right\} \\ &= \omega_f \left(\frac{2}{m}; [-1, 1]^d \right). \end{aligned} \quad (18)$$

By substituting (18) into (17), we get the claimed upper bound.

For estimating $\|\tilde{V}_m\|_{L_\infty}$, it is straightforward to see that $\|\tilde{V}_m\|_{L_\infty} = 1$ by multi-binomial theorem

$$\begin{aligned} &\|\tilde{V}_m(f)\|_{L_\infty([-1, 1]^d)} \\ &\leq \|f\|_{L_\infty([-1, 1]^d)} \sum_{k_1=0}^m \cdots \sum_{k_d=0}^m \binom{m}{k_1} \cdots \binom{m}{k_d} \\ &\quad \times \prod_{i=1}^d \left(\left(\frac{z_i + 1}{2}\right)^{k_i} \left(\frac{1 - z_i}{2}\right)^{m-k_i} \right) \\ &= \|f\|_{L_\infty([-1, 1]^d)}. \end{aligned}$$

□

Theorem C.6. *Let $\mathcal{X}, \mathcal{Y} \subset \mathcal{C}([-1, 1]^d)$ and $\mathcal{M} : \mathcal{X} \rightarrow \mathcal{Y}$. Suppose that Assumption 4.1 and Assumption 4.2 hold. Then we have for any $f \in \mathcal{X}$,*

$$\begin{aligned} &\|\mathcal{M}(f) - V_m \circ \mathcal{M} \circ V_m(f)\|_{L_\infty} \\ &\leq 6L_\mathcal{M} d^2 \omega_f \left(\frac{2}{m}; [-1, 1]^d \right) + \frac{5L_\mathcal{Y} d}{2m}. \end{aligned}$$

Proof of Theorem C.6. To begin with, we present the subsequent error decomposition

$$\begin{aligned} &\|\mathcal{M}(f) - V_m \circ \mathcal{M} \circ V_m(f)\|_{L_\infty} \\ &\leq \underbrace{\|\mathcal{M}(f) - \mathcal{M} \circ V_m(f)\|_{L_\infty}}_{(i)} \\ &\quad + \underbrace{\|\mathcal{M} \circ V_m(f) - V_m \circ \mathcal{M} \circ V_m(f)\|_{L_\infty}}_{(ii)}. \end{aligned} \quad (19)$$

For the term (i), we can derive

$$(i) \leq L_\mathcal{M} \|f - V_m(f)\|_{L_\infty} \leq \frac{5L_\mathcal{M} d}{4} \omega_f \left(\frac{2}{m}; [-1, 1]^d \right), \quad (20)$$

where we use Lemma C.5 and Lipschitz property of \mathcal{M} in Assumption 4.1.

Since $\mathcal{M} \circ V_m(f) \in \mathcal{C}([-1, 1]^d)$, applying Lemma C.5 again to the second term (ii), we derive

$$\begin{aligned} &\|\mathcal{M} \circ V_m(f) - V_m \circ \mathcal{M} \circ V_m(f)\|_{L_\infty([-1, 1]^d)} \\ &\leq \frac{5d}{4} \omega_{\mathcal{M} \circ V_m(f)} \left(\frac{2}{m}; [-1, 1]^d \right). \end{aligned} \quad (21)$$

Now we need to estimate $\omega_{\mathcal{M} \circ V_m(f)}$. Lemma C.5, As-

sumption 4.1, and Assumption 4.2 jointly imply that

$$\begin{aligned}
& |\mathcal{M} \circ V_m(f)(x_1) - \mathcal{M} \circ V_m(f)(x_2)| \\
& \leq |\mathcal{M} \circ V_m(f)(x_1) - \mathcal{M}(f)(x_1)| \\
& \quad + |\mathcal{M}(f)(x_1) - \mathcal{M}(f)(x_2)| \\
& \quad + |\mathcal{M}(f)(x_2) - \mathcal{M} \circ V_m(f)(x_2)| \\
& \leq 2\|\mathcal{M} \circ V_m(f) - \mathcal{M}(f)\|_{L_\infty} + L_Y\|x_1 - x_2\|_2 \\
& \leq 2L_\mathcal{M}\|V_m(f) - f\|_{L_\infty} + L_Y\|x_1 - x_2\|_2 \\
& \leq \frac{10L_\mathcal{M}d}{4}\omega_f\left(\frac{2}{m}; [-1, 1]^d\right) + L_Y\|x_1 - x_2\|_2.
\end{aligned}$$

Substituting the above inequality into the definition of $\omega_{\mathcal{M} \circ V_m(f)}$, we obtain

$$\begin{aligned}
& \omega_{\mathcal{M} \circ V_m(f)}\left(\frac{2}{m}; [-1, 1]^d\right) \\
& = \left\{ |\mathcal{M} \circ V_m(f)(x_1) - \mathcal{M} \circ V_m(f)(x_2)| : \|x_1 - x_2\|_2 \leq \frac{2}{m}, \right. \\
& \quad \left. x_1, x_2 \in [-1, 1]^d \right\} \\
& \leq \frac{10L_\mathcal{M}d}{4}\omega_f\left(\frac{2}{m}; [-1, 1]^d\right) + \frac{2L_Y}{m}.
\end{aligned}$$

Hence, combining (21) with the above estimation of $\omega_{\mathcal{M} \circ V_m(f)}$, the second term (ii) is bounded by

$$(ii) \leq \frac{25L_\mathcal{M}d^2}{8}\omega_f\left(\frac{2}{m}; [-1, 1]^d\right) + \frac{5L_Yd}{2m}. \quad (22)$$

We finally get the upper bound by substituting (20) and (22) into (19)

$$\begin{aligned}
& \|\mathcal{M}(f) - V_m \circ \mathcal{M} \circ V_m(f)\|_{L_\infty} \\
& \leq 6L_\mathcal{M}d^2\omega_f\left(\frac{2}{m}; [-1, 1]^d\right) + \frac{5L_Yd}{2m}.
\end{aligned}$$

We finish the proof. \square

Theorem C.6 demonstrates that as m approaches infinity, the expression $\mathcal{M} \rightarrow V_m \circ \mathcal{M} \circ V_m$ converges uniformly on \mathcal{X} . The concept of V_m implies that in practical applications, when handling data, it is necessary to convert a continuous signal into a finite-dimensional vector. Since V_m produces polynomials up to degree m , which constitutes a finite-dimensional space, this space is consequently learnable. Thus, we consider the use of U-shaped networks to approximate $V_m \circ \mathcal{M} \circ V_m$. If this approximation approaches zero, it means that U-architectures possess the universal approximation property.

We now introduce some fundamental concepts that will be used later. We define Legendre polynomials as

$$P_n(x) := \frac{(-1)^n \sqrt{n+1/2}}{2^n n!} \left(\frac{d}{dx}\right)^n \{(1-x^2)^n\}.$$

For $x = (x_1, \dots, x_d)^\top \in \mathbb{R}^d$, we define

$$P_{\mathbf{k}}(x) = \prod_{j=1}^d P_{k_j}(x_j),$$

where $\mathbf{k} := (k_1, \dots, k_d) \in \mathbb{R}^d$. Notice that we have

$$\langle P_{\mathbf{k}_1}, P_{\mathbf{k}_2} \rangle = \delta_{\mathbf{k}_1, \mathbf{k}_2},$$

where $\delta_{\mathbf{k}_1, \mathbf{k}_2} = 1$ if $\mathbf{k}_1 = \mathbf{k}_2$ and zero otherwise. Without loss of generality, we replace the multi-index with the scalar index, i.e., $\{P_{\mathbf{k}} : \mathbf{k} \in \{0, 1, 2, \dots, m\}^d\} = \{P_k\}_{k=1}^{(m+1)^d}$. Obviously $\{P_k\}_{k=1}^{(m+1)^d}$ forms a basis of the polynomial space Π_m .

We introduce an isometric isomorphism mapping $\phi : \Pi_m \rightarrow \mathbb{R}^{(m+1)^d}$:

$$\phi(Q) := (\langle Q, P_1 \rangle, \dots, \langle Q, P_t \rangle)^\top,$$

where $t := (m+1)^d$ and $Q \in \Pi_m$. Then we can see that for any $\hat{Q} \in \mathbb{R}^t$

$$\phi^{-1}(\hat{Q}) := \sum_{i=1}^t \hat{Q}_i P_i,$$

satisfies

$$\begin{aligned}
\phi^{-1}\phi(Q) &= Q \\
\|Q\|_{L_2}^2 &= \|\hat{Q}\|_2^2.
\end{aligned}$$

Hence we can rewrite $V_m \circ \mathcal{M} \circ V_m$ as

$$V_m \circ \mathcal{M} \circ V_m = \phi^{-1} \circ (\phi \circ V_m \circ \mathcal{M} \circ \phi^{-1}) \circ \phi \circ V_m(f),$$

for further analysis. Here we have that $\phi \circ V_m \circ \mathcal{M} \circ \phi^{-1} : \mathbb{R}^t \rightarrow \mathbb{R}^t$ is a mapping between finite dimensional spaces and ϕ encodes the information of the function $V_m f$ into a vector and ϕ^{-1} decodes the information from a vector into a continuous function.

The following lemma is a useful property for characterizing norms of polynomials.

Lemma C.7 ([43]). *Let $p, q \in [1, \infty]$, then for any $m \in \mathbb{N}$ and $Q \in \Pi_m$, we have*

$$\|Q\|_{L_p([-1, 1]^d)} \leq c \cdot m^{2d \max\{\frac{1}{q} - \frac{1}{p}, 0\}} \|Q\|_{L_q([-1, 1]^d)},$$

where c is a constant and independent of m .

The following lemma shows that $\phi \circ V_m \circ \mathcal{M} \circ \phi^{-1}$ is Lipschitz.

Lemma C.8. *Suppose Assumption 4.1 holds. The mapping $\phi \circ V_m \circ \mathcal{M} \circ \phi^{-1} : \mathbb{R}^t \rightarrow \mathbb{R}^t$ is Lipschitz, that is,*

$$\begin{aligned}
& \|\phi \circ V_m \circ \mathcal{M} \circ \phi^{-1}(w_1) - \phi \circ V_m \circ \mathcal{M} \circ \phi^{-1}(w_2)\|_\infty \\
& \leq cL_\mathcal{M}m^d\|w_1 - w_2\|_2,
\end{aligned}$$

for any $w_1, w_2 \in \mathbb{R}^t$.

Proof. Let $w_1, w_2 \in \mathbb{R}^t$. Then we have

$$\begin{aligned} & \|\phi \circ V_m \circ \mathcal{M} \circ \phi^{-1}(w_1) - \phi \circ V_m \circ \mathcal{M} \circ \phi^{-1}(w_2)\|_\infty \\ & \leq \|\phi \circ V_m \circ \mathcal{M} \circ \phi^{-1}(w_1) - \phi \circ V_m \circ \mathcal{M} \circ \phi^{-1}(w_2)\|_2 \\ & = \|V_m \circ \mathcal{M} \circ \phi^{-1}(w_1) - V_m \circ \mathcal{M} \circ \phi^{-1}(w_2)\|_{L_2} \\ & \leq c \|V_m \circ \mathcal{M} \circ \phi^{-1}(w_1) - V_m \circ \mathcal{M} \circ \phi^{-1}(w_2)\|_{L_\infty} \\ & \leq c L_{\mathcal{M}} \|\phi^{-1}(w_1) - \phi^{-1}(w_2)\|_{L_\infty} \\ & \leq c L_{\mathcal{M}} m^d \|\phi^{-1}(w_1) - \phi^{-1}(w_2)\|_{L_2} \\ & = c L_{\mathcal{M}} m^d \|w_1 - w_2\|_2, \end{aligned}$$

where in the first step we use $\|z\|_\infty \leq \|z\|_2$ for any $z \in \mathbb{R}^t$, in the second step we use the definition of ϕ , in the third step we use Lemma C.7, in the fourth step we use Assumption 4.1 and Lemma C.5, in the fifth step we use Lemma C.7, and in the last step we use the definition of ϕ^{-1} . \square

For any Lipschitz mapping, it is possible to identify a CNN where the approximation error remains sufficiently small. This conclusion is presented in the following lemma.

Lemma C.9. *Let $L, N \in \mathbb{N}_+$ with $N > t^{t/(t-1)}$. Suppose Assumption 4.1 holds. Then there exists a CNN Φ with depth $O(L \log(tN))$ and total number of parameters $O(Lt^2N^2)$ such that*

$$\begin{aligned} & \|\phi \circ V_m \circ \mathcal{M} \circ \phi^{-1}(w) - \Phi(w)\|_\infty \\ & \leq CL_{\mathcal{M}} m^d (N^2 L^2 \log(N))^{-1/t}, \end{aligned}$$

for any $w \in [-1, 1]^t$ where C is a positive constant.

Proof. Let $L, N \in \mathbb{N}_+$ with $N > t^{t/(t-1)}$. Given a Lipschitz function f with Lipschitz constant λ , [53, Corollary 1.3] implies that there exists a ReLU neural network ψ with depth $O(L)$ and width $O(N)$ such that

$$\|f - \psi\|_{L_\infty([-1, 1]^d)} \leq C \lambda (N^2 L^2 \log(N))^{-1/t},$$

where C depends only on d .

Consider f_i as Lipschitz functions, where $i \in [t]$. Using [60, Proposition 4.1], we can then approximate the following mapping

$$F(x) := \begin{pmatrix} f_1(x) \\ f_2(x) \\ \dots \\ f_t(x) \end{pmatrix}$$

by using a ReLU neural network $\Psi : \mathbb{R}^t \rightarrow \mathbb{R}^t$ which has depth $O(L)$ and width $O(tN)$ such that

$$\sup_{x \in [-1, 1]^t} \|F(x) - \Psi(x)\|_\infty \leq C \lambda (N^2 L^2 \log(N))^{-1/t},$$

for a constant $C > 0$ that depends only on d . Since any affine transformation from \mathbb{R}^N to \mathbb{R}^N can be represented by no more than $O(\log N)$ convolutional layers with a total number of parameters at most N^2 [35], we can construct a convolutional neural network Φ with depth $O(L \log(tN))$ and total number of parameters $O(Lt^2N^2)$ such that $\Phi = \Psi$ and

$$\sup_{x \in [-1, 1]^t} \|F(x) - \Phi(x)\|_\infty \leq C \lambda (N^2 L^2 \log(N))^{-1/t}.$$

Since Lemma C.8 implies that $\phi \circ V_m \circ \mathcal{M} \circ \phi^{-1}$ is a special case of F , we can conclude the proof by setting $\lambda := c L_{\mathcal{M}} m^d$. \square

To approximate ϕ and ϕ^{-1} , an error analysis can be conducted on a collection of sample points within $[-1, 1]^d$ by employing the two lemmas outlined below.

Lemma C.10. *There exists $\xi_{\text{in}} = \{\xi_i\}_{i=1}^t \subset [-1, 1]^d$ such that we can find a CNN Φ_{in} with depth $O(\log t)$ and total number of parameters $O(t^2)$, satisfying*

$$\Phi_{\text{in}}(S(Q, \xi_{\text{in}})) = \phi(Q), \quad \forall Q \in \Pi_m.$$

Proof. Since $P_i \in \Pi_m$, $i = 1, \dots, t$ are multidimensional Legendre polynomials which are constructed by the tensor products of univariate orthonormal Legendre polynomials with degree no more than m , by using [15, Theorem 14.2.1], there exists $\xi = \{\xi_1, \dots, \xi_t\} \subset [-1, 1]^t$ and positive weights $w_i > 0$, $i = 1, \dots, t$ such that

$$\int_{[-1, 1]^d} Q(x) P_i(x) dx = \sum_{j=1}^t w_j Q(\xi_j) P_i(\xi_j), \quad \forall Q \in \Pi_m.$$

Let us define

$$U = \begin{pmatrix} w_1 P_1(\xi_1) & w_2 P_1(\xi_2) & \dots & w_t P_1(\xi_t) \\ \vdots & \ddots & \ddots & \vdots \\ w_1 P_i(\xi_1) & w_2 P_i(\xi_2) & \dots & w_t P_i(\xi_t) \\ \vdots & \ddots & \ddots & \vdots \\ w_1 P_t(\xi_1) & w_2 P_t(\xi_2) & \dots & w_t P_t(\xi_t) \end{pmatrix}.$$

Then it is obvious that

$$U S(Q, \xi) = \phi(Q).$$

Using [35], there exists a CNN Φ_{in} with depth $O(\log t)$ and total number of parameters $O(t^2)$ such that

$$\Phi_{\text{in}}(S(Q, \xi)) = U S(Q, \xi).$$

\square

Lemma C.11. Given any $\xi_{\text{out}} = \{\xi_i\}_{i=1}^t \subset [-1, 1]^d$, there exists a CNN Φ_{out} with depth $O(\log t)$ and total number of parameters $O(t^2)$, satisfying

$$\Phi_{\text{out}}(\phi(Q)) = S(Q, \xi_{\text{out}}), \forall Q \in \Pi_m.$$

In addition, Φ_{out} is Lipschitz, i.e.,

$$\|\Phi_{\text{out}}(w) - \Phi_{\text{out}}(z)\|_{\infty} \leq Ct^2\|w - z\|_{\infty},$$

for any $w, z \in \mathbb{R}^t$.

Proof. Define

$$P = \begin{pmatrix} P_1(\xi_1) & P_2(\xi_1) & \dots & P_t(\xi_1) \\ \vdots & \ddots & \ddots & \vdots \\ P_1(\xi_t) & P_2(\xi_t) & \dots & P_t(\xi_t) \\ \vdots & \ddots & \ddots & \vdots \\ P_1(\xi_t) & P_2(\xi_t) & \dots & P_t(\xi_t) \end{pmatrix}.$$

Then we can see that

$$S(Q, \xi) = \sum_{i=1}^t \langle Q, P_i \rangle S(P_i, \xi) = P\phi(Q).$$

Using [35], there exists a CNN Φ_{out} with depth $O(\log t)$ and total number of parameters $O(t^2)$ such that

$$\Phi_{\text{out}}(\phi(Q)) = S(Q, \xi) = P\phi(Q).$$

Furthermore, since Lemma C.7 indicates that for any $j \in \{1, \dots, t\}$, $\|P_j\|_{L_{\infty}([-1, 1]^d)} \leq Cm^d$, we can obtain that Φ_{out} is Lipschitz

$$\begin{aligned} \|\Phi_{\text{out}}(w) - \Phi_{\text{out}}(z)\|_{\infty} &\leq t \sup_j \|P_j\|_{L_{\infty}} \|w - z\|_{\infty} \\ &\leq Ct^2\|w - z\|_{\infty}, \end{aligned}$$

where we use the definition of ∞ -matrix norm. \square

We are now prepared to demonstrate the primary result.

Theorem C.12. Let $d, m, L, K \in \mathbb{N}_+$, $t = (m + 1)^d$ and $\Omega = [-1, 1]^d$. Let $\mathcal{X} \subset \{f \in \mathcal{C}(\Omega) : \|f\|_{L_{\infty}} \leq 1\}$. Suppose Assumption 4.1 and Assumption 4.2 hold. Then, there exists a linear mapping $V_m : \mathcal{C}(\Omega) \rightarrow \Pi_m$ and a set of points $\xi_{\text{in}} \subset \Omega$ with $|\xi_{\text{in}}| = t$ such that for any $\xi_{\text{out}} \subset \Omega$ with $|\xi_{\text{out}}| = t$, we can find a U-shaped network $\Phi \in \mathcal{U}(O(L \log(tK)), O(t^2K))$, satisfying

$$\|S(\mathcal{M}(f), \xi_{\text{out}}) - \Phi(S(V_m(f), \xi_{\text{in}}))\|_{\infty} \quad (23)$$

$$\leq C_1 \omega_f \left(\frac{2}{m} \right) + \frac{C_2}{m} + \frac{C_3 t^3}{(LK \log(K/L))^{1/t}}, \quad (24)$$

for any $f \in \mathcal{X}$. Here, $C_1, C_2, C_3 > 0$ depend on $d, L_{\mathcal{M}}, L_{\mathcal{Y}}$.

Proof. Theorem C.6 implies that

$$\begin{aligned} &\|S(\mathcal{M}(f) - V_m \circ \mathcal{M} \circ V_m(f), \xi_{\text{out}})\|_{\infty} \\ &\leq 6L_{\mathcal{M}} d^2 \omega_f \left(\frac{2}{m}; [-1, 1]^d \right) + \frac{5L_{\mathcal{Y}} d}{2m}. \end{aligned} \quad (25)$$

Applying Lemma C.10, we get a CNN Φ_{in} with depth $O(\log t)$ and total number of parameters $O(t^2)$ such that

$$\begin{aligned} &V_m \circ \mathcal{M} \circ V_m(f) \\ &= \phi^{-1} \circ (\phi \circ V_m \circ \mathcal{M} \circ \phi^{-1}) \circ \phi \circ V_m(f) \\ &= \phi^{-1} \circ (\phi \circ V_m \circ \mathcal{M} \circ \phi^{-1}) \circ \Phi_{\text{in}}(S(V_m(f), \xi_{\text{in}})) \end{aligned} \quad (26)$$

since $V_m(f) \in \Pi_m$. By the definition of ϕ , we have

$$\begin{aligned} \|\phi \circ V_m(f)\|_{\infty} &\leq \|\phi \circ V_m(f)\|_2 \leq \|V_m(f)\|_{L_2} \\ &\leq c\|V_m(f)\|_{L_{\infty}} \leq c\|f\|_{L_{\infty}}, \end{aligned}$$

where we use Lemma C.7 in the third step and Lemma C.5 in the last step. Hence we also have

$$\|\Phi_{\text{in}}(S(V_m(f), \xi_{\text{in}}))\|_{\infty} \leq c\|f\|_{L_{\infty}} \leq c, \forall \|f\|_{\infty} \leq 1. \quad (27)$$

Lemma C.11 implies that we can find a CNN Φ_{out} with depth $O(\log t)$ and total number of parameters $O(t^2)$ such that $\Phi_{\text{out}}(\phi(Q)) = S(Q, \xi_{\text{out}})$ for any $Q \in \Pi_m$. Substituting this fact into (26) and using the definition of ϕ^{-1} yield

$$\begin{aligned} &S(V_m \circ \mathcal{M} \circ V_m(f), \xi_{\text{out}}) \\ &= \Phi_{\text{out}} \circ (\phi \circ V_m \circ \mathcal{M} \circ \phi^{-1}) \circ \Phi_{\text{in}}(S(V_m(f), \xi_{\text{in}})). \end{aligned} \quad (28)$$

The rest part is to construct a bottleneck Φ_{bot} for approximating $\phi \circ V_m \circ \mathcal{M} \circ \phi^{-1}$. Lemma C.9 indicates that there exists a CNN Φ_{bot} with depth $O(L \log(tN))$ and total number of parameters $O(Lt^2N^2)$ such that

$$\begin{aligned} &\sup_{w \in [-1, 1]^t} \|\phi \circ V_m \circ \mathcal{M} \circ \phi^{-1}(w) - \Phi_{\text{bot}}(w)\|_{\infty} \\ &\leq CL_{\mathcal{M}} m^d (N^2 L^2 \log(N))^{-1/t}. \end{aligned}$$

Hence the following inequalities hold

$$\begin{aligned} &\|\Phi_{\text{out}} \circ (\phi \circ V_m \circ \mathcal{M} \circ \phi^{-1}) \circ \Phi_{\text{in}}(S(V_m(f), \xi_{\text{in}})) \\ &\quad - \Phi_{\text{out}} \circ \Phi_{\text{bot}} \circ \Phi_{\text{in}}(S(V_m(f), \xi_{\text{in}}))\|_{\infty} \\ &\leq Ct^2 \sup_{w \in [-c, c]^t} \|\phi \circ V_m \circ \mathcal{M} \circ \phi^{-1}(w) - \Phi_{\text{bot}}(w)\|_{\infty} \\ &\leq Ct^2 L_{\mathcal{M}} m^d (N^2 L^2 \log(N))^{-1/t}. \end{aligned} \quad (29)$$

where in the first step we use Lemma C.11 and in the second step we use Lemma C.9 and (27). Here we can apply Lemma C.9 since the corresponding proof can be easily adapted to domain $[-c, c]^t$.

Let $\Phi := \Phi_{\text{out}} \circ \Phi_{\text{bot}} \circ \Phi_{\text{in}}$. Combining (28), (25), and (29), we obtain

$$\begin{aligned} & \|S(\mathcal{M}(f), \xi_{\text{out}}) - \Phi(S(V_m(f), \xi_{\text{in}}))\|_{\infty} \\ & \leq \|S(\mathcal{M}(f) - V_m \circ \mathcal{M} \circ V_m(f), \xi_{\text{out}})\|_{\infty} \\ & \quad + \|S(V_m \circ \mathcal{M} \circ V_m, \xi_{\text{out}}) - \Phi(S(V_m(f), \xi_{\text{in}}))\|_{\infty} \\ & \leq 6L_{\mathcal{M}}d^2\omega_f \left(\frac{2}{m}; [-1, 1]^d \right) + \frac{5L_{\mathcal{Y}}d}{2m} \\ & \quad + CL_{\mathcal{M}} \frac{t^3}{(N^2 L^2 \log(N))^{1/t}}, \end{aligned}$$

where Φ is a CNN with depth $O(\log t + L \log(tN)) = O(L \log(tN))$ and total number of parameters $O(t^2 + t^2 LN^2) = O(t^2 LN^2)$. Let $K = LN^2$, then we finish the proof. \square

In the following, we offer a comprehensive analysis of the outcomes presented in the theorem.

The role of V_m . The linear operator V_m transforms a continuous function into the space of polynomials. According to the Stone-Weierstrass theorem, polynomials are dense in $C(\Omega)$. Therefore, substituting samples of f with samples of $V_m(f)$ is adequate, provided that m is sufficiently large.

The role of ξ_{in} . In our analysis, we select a particular set of points to capture the information from a continuous function. Given that a finite number of sample locations can specify any polynomial in Π_m , sampling enough points allows us to completely represent $V_m(f)$.

The role of ξ_{out} . U-shaped networks cannot generate functions as outputs, so we analyze the error between $\mathcal{M}(f)$ and $\Phi(S(V_m(f), \xi_{\text{in}}))$ at the set of output locations ξ_{out} . With ξ_{out} fixed, Theorem 4.3 provides an effective network for these specific points. However, if the function's smoothness is inadequate, the same neural network might not perform well at other points.

C.6 Proof of Theorem 4.4

We first need to establish the relationship between U-shaped networks and fully connected neural networks. Fully connected neural networks are defined as

$$\Psi = \mathcal{A}_L \circ \sigma \circ \mathcal{A}_{L-1} \circ \dots \circ \sigma \circ \mathcal{A}_1,$$

where $\mathcal{A}_\ell(z) = A_\ell \cdot z + b_\ell$, involving a weight matrix A_ℓ and a bias vector b_ℓ . We define L as the number of layers within Ψ and represent K as the total number of non-zero parameters in the weight matrices and bias vectors of \mathcal{A}_ℓ , $\ell \in [L]$. We denote $\mathcal{NN}(L, K)$ as the collection of all fully connected neural networks with no more than L layers and at most K nonzero parameters. Then we can show that U-shaped networks can be viewed as special fully connected neural networks.

Lemma C.13. *Let $L, K \in \mathbb{N}_+$ and $\mathcal{U}(L, K), \mathcal{NN}(L, K)$ be the collection of U-shaped networks and fully connected networks defined on \mathbb{R}^t . Then $\mathcal{U}(L, K) \subset \mathcal{NN}(L, \max\{tK, K^2\})$.*

Proof. Let $x \in \mathbb{R}^{n_1 \times c_1}$ be a tensor with c channels and each channel be denoted as $x_i \in \mathbb{R}^{n_1}$. Given a set of kernels $w_{\ell, i} \in \mathbb{R}^2$, $\ell \in [c_2]$, $i \in [c_1]$, the convolution between x and these kernels is given by

$$y_\ell = \sum_{i=1}^{c_1} w_{\ell, i} *_2 x_i = \sum_{i=1}^{c_1} T^{w_{\ell, i}} x_i,$$

where $y \in \mathbb{R}^{\lceil n_1/2 \rceil \times c_2}$ and $T^{w_{\ell, i}} \in \mathbb{R}^{\lceil n_1/2 \rceil \times n_1}$ with at most $2\lceil n_1/2 \rceil \leq n_1 + 2$ nonzero entries. Denote

$$\tilde{x} := \begin{pmatrix} x_1 \\ \vdots \\ x_{c_1} \end{pmatrix}, \quad \tilde{y} := \begin{pmatrix} y_1 \\ \vdots \\ y_{c_2} \end{pmatrix}$$

and

$$\tilde{T} := \begin{pmatrix} T^{w_{1,1}} & T^{w_{1,2}} & \dots & T^{w_{1,c_1}} \\ T^{w_{2,1}} & T^{w_{2,2}} & \dots & T^{w_{2,c_1}} \\ \vdots & \vdots & \ddots & \vdots \\ T^{w_{c_2,1}} & T^{w_{c_2,2}} & \dots & T^{w_{c_2,c_1}} \end{pmatrix}.$$

Obviously we have $\tilde{y} = \tilde{T}\tilde{x}$ and in \tilde{T} there are at most $(n_1 + 2) \times c_1 \times c_2$ parameters.

Meanwhile, there are $2c_1c_2$ parameters in the set of kernels $w_{\ell, i} \in \mathbb{R}^2$, $\ell \in [c_2]$, $i \in [c_1]$. Thus, we can always rewrite any convolution operation into an affine mapping with nonzero parameters no more than the parameters in convolutional kernels times the dimension of each channel of inputs. In U-shaped networks, this is no greater than $\max\{t, K\}$. If there is no flatten operation during the feed-forward processing, the stride-2 convolution with kernel size 2 will always produce smaller dimensions in each channel. Hence, this might exceed $\max\{t, K\}$ only when there is a flatten operation. Before the flatten operation, we will get a tensor with each channel having dimension 1. If this tensor has more than K channels, the convolution layer to produce this tensor has at least K convolution kernels which have $2K$ parameters. However, K represent the overall number of parameters in U-shaped networks. This presents a contradiction, suggesting that the output dimension of each layer does not exceed $\max\{t, K\}$. Consequently, the fully connected network formed has at most $\max\{tK, K^2\}$ parameters. Thus, the proof is complete. \square

Theorem C.14. *Let $d, m \in \mathbb{N}_+$ and $t = (m+1)^d$. Let $\mathcal{M} : \Pi_m \rightarrow \Pi_m$ and $\mathcal{X} = \Pi_m$. Suppose that Assumption 4.1*

holds. Then there exists $\xi_{\text{in}}, \xi_{\text{out}} \subset [-1, 1]^d$ with $|\xi_{\text{in}}| = |\xi_{\text{out}}| = t$ and a constant $C > 0$ such that

$$\begin{aligned} & \inf_{\Phi \in \mathcal{U}(L, K)} \sup_{f \in \mathcal{X}} \|S(\mathcal{M}(f), \xi_{\text{out}}) - \Phi(S(f, \xi_{\text{in}}))\|_{\infty} \\ & \geq C(tK^2 L \log(tK^2))^{-1/t}. \end{aligned} \quad (30)$$

Proof. Since $\mathcal{M} : \Pi_m \rightarrow \Pi_m$, we can write

$$\mathcal{M}(f) = \phi^{-1} \circ (\phi \circ \mathcal{M} \circ \phi^{-1}) \circ \phi(f), \quad (31)$$

for any $f \in \Pi_m$. Using a similar approach as the proof of Lemma C.8, we can show that $\phi \circ \mathcal{M} \circ \phi^{-1}$ is Lipschitz. Lemma C.10 and Lemma C.11 implies that by setting $\xi_{\text{out}} := \xi_{\text{in}}$, for any $f \in \Pi_m$, there exist two matrices $P, U \in \mathbb{R}^{t \times t}$ such that

$$\begin{aligned} US(f, \xi_{\text{in}}) &= \phi(f), \\ S(f, \xi_{\text{out}}) &= P\phi(f). \end{aligned}$$

Replacing these equalities into (31), we can represent \mathcal{M} over sample location set ξ_{out} as

$$S(\mathcal{M}(f), \xi_{\text{out}}) = P \circ (\phi \circ \mathcal{M} \circ \phi^{-1}) \circ U(S(f, \xi_{\text{in}})).$$

Let $F(\cdot) := P \circ (\phi \circ \mathcal{M} \circ \phi^{-1}) \circ U(\cdot)$. Obviously F is Lipschitz.

We denote $\mathcal{NN}(L, K_2)$ with $K_2 := \max\{tK, K^2\}$. Using Lemma C.13, we obtain

$$\begin{aligned} & \inf_{\Phi \in \mathcal{U}(L, K)} \sup_{f \in \mathcal{X}} \|S(\mathcal{M}(f), \xi_{\text{out}}) - \Phi(S(f, \xi_{\text{in}}))\|_{\infty} \\ &= \inf_{\Phi \in \mathcal{U}(L, K)} \sup_{f \in \mathcal{X}} \|F(S(f, \xi_{\text{in}})) - \Phi(S(f, \xi_{\text{in}}))\|_{\infty} \\ &\geq \inf_{\Phi \in \mathcal{NN}(L, K_2)} \sup_{x \in [-1, 1]^d} \|F(x) - \Phi(x)\|_{\infty} \\ &\geq \inf_{\Phi \in \mathcal{NN}(L, K_2)} \|F_1(x) - \Phi_1(x)\|_{L_{\infty}}, \end{aligned} \quad (32)$$

where we use the notation $F(\cdot) := (F_1(\cdot), \dots, F_t(\cdot))^{\top}$ and $\Phi(\cdot) := (\Phi_1(\cdot), \dots, \Phi_t(\cdot))^{\top}$.

Since F_1 is a Lipschitz function, we can use [53, Theorem 2.4] and [5] to get the lower bound when using fully connected neural networks for approximation

$$\inf_{\Phi \in \mathcal{NN}(L, K_2)} \|F_1(x) - \Phi_1(x)\|_{L_{\infty}} \geq C(K_2 L \log K_2)^{-1/t}, \quad (33)$$

where C only depends on t . Substituting (33) into (32), we finally obtain

$$\begin{aligned} & \inf_{\Phi \in \mathcal{U}(L, K)} \sup_{f \in \mathcal{X}} \|S(\mathcal{M}(f), \xi_{\text{out}}) - \Phi(S(f, \xi_{\text{in}}))\|_{\infty} \\ &\geq C(tK^2 L \log(tK^2))^{-1/t}. \end{aligned}$$

We complete the proof. \square

Theorem 4.4 suggests that even if we restrict \mathcal{M} to act as a mapping between finite-dimensional subsets of $\mathcal{C}(\Omega)$, we cannot expect a significant enhancement. Once the network architecture is fixed, there will always be a lower bound.

Theorem 4.3 and Theorem 4.4 jointly offer a significant understanding of $B_{\alpha}(\Phi(\cdot))$. According to Definition 3.1, hallucination occurs when $\mathcal{M}(X) \notin B_{\alpha}(\Phi(X))$. Our theoretical findings indicate several factors that could lead to hallucination: (i) the intrinsic natures of real world scenes; (ii) the discretization process; (iii) the expressivity of the network. These factors also indicate that hallucination might be a universal problem in machine learning.

Remark C.15. Theoretical Perspectives on U-Shaped Networks: While recent research has aimed to improve the performance of U-Nets, a complete theoretical explanation of their effectiveness remains elusive. Recent efforts to clarify its representational power have focused on interpretative views of the architecture. The learning task has been formulated as a PDE-constrained optimal control problem, where the U-Net corresponds to a single iteration of a hybrid operator-splitting scheme [56]. Another interpretation shows that the U-Net structure arises from the decomposition of a Hankel matrix associated with sparse-view CT data, establishing a connection between deep learning and compressed sensing via deep convolutional framelets [22]. It has also been shown that U-Net's architecture can implement the belief propagation algorithm on generative hierarchical models, i.e. tree-structured graphical models, thereby efficiently approximating denoising functions [42]. Finally, a general framework for designing and analyzing U-Net architectures highlights the distinct roles of the encoder and decoder [59].